

> REPLACE THIS LINE WITH YOUR MANUSCRIPT ID NUMBER (DOUBLE-CLICK HERE TO EDIT) <

Safety-Quantifiable Planar-Feature-based LiDAR Localization with a Prior Map for Intelligent Vehicles in Urban Scenarios

Jiachen Zhang, Xikun Liu, Weisong Wen*, and Li-Ta Hsu

Abstract—Safety-quantifiable and accurate localization is of great importance for safety-critical applications with navigation requirements, such as intelligent vehicles (IV). LiDAR-based localization with the prior map is highly expected due to its high accuracy. However, how to reliably quantify the safety (quantify the maximum potential localization error) of LiDAR localization is still an open challenge. Integrity monitoring (IM) is one of the most stringent existing solutions to quantify the safety of satellite navigation, where usually tens of measurements are involved and interpreted by an almost locally linear model. Differently, the number of measurements involved in the LiDAR localization problem is significantly larger (e.g. 2000). Moreover, the LiDAR measurement model is highly non-linear. The convexity of the LiDAR localization is still to be quantified. To fill these gaps, this paper proposes a safety-quantifiable planar feature-based LiDAR localization method with a prior map. Specifically, the LiDAR localization framework utilizing representative planar features with maximum spectral attributes is proposed. The cardinality restriction facilitates feasible safety quantification regardless of thousands of measurements. To quantify the convexity of the LiDAR localization problem, the Hessian matrix of the planar feature measurement model is analytically derived. The local convex property during non-linear optimization of the localization model is quantified from dual perspectives. Additionally, different from existing methods, the protection level of the derived LiDAR localization is estimated for both translation and rotation to quantify the safety. The feasibility of the proposed method is validated using the datasets collected in typical urban canyons of Hong Kong.

Index Terms—3D LiDAR; Non-convexity; Planar features, Safety-quantifiable Localization; Urban canyons.

I. INTRODUCTION

A. Motivation

Localization is one of the key prerequisites for intelligent vehicles (IV) [1]. Light detection and ranging (LiDAR) gains increasing popularity due to its high reliability and precision [2]. With the help of the precise prebuilt 3D point cloud map, centimeter-level accuracy can be obtained by feature-based LiDAR localization [3]. However, as shown in our previous work in [4], the performance of LiDAR localization is significantly challenged in urban canyons, due to the numerous unexpected moving objects, insufficient geometric features, etc. Researchers tend to improve the robustness and accuracy

through sensor fusion [5], robust estimation [6], etc. However, hardly any existing feature-based LiDAR localization method confirms the safety in a real-world test. Reliable safety quantification of the localization results is of great significance for IV to guarantee the passengers' physical safety. Without safety quantification, hazardous operations consequently could occur. Such concern partly prevents the massive deployment of safety-critical intelligent applications [7].

The safety quantification of the localization solution requires awareness of the potential maximum localization error. Although safety concepts have been defined by ISO 26262 [8], the safety issue has not been effectively tackled. For example, what would the noise of the LiDAR measurements lead to the potential localization error? How would the potential undetected LiDAR outlier measurements contribute to the potential localization error and how to quantify it?

Interestingly, integrity monitoring (IM) was developed for the aviation industry as the safety quantification theory. Specifically, integrity is introduced to quantify the trust that can be placed in the correctness of the position information provided by the Global Navigation Satellite System (GNSS) [9]. IM is implemented mainly in two steps [10]. First, fault detection and exclusion (FDE) are performed. In particular, faulty measurements that exhibit significant inconsistency with other measurements are detected and excluded. However, some faults that are not readily noticeable but potentially exist could result in a potential error in the position estimation. In addition, the noise contained in the GNSS measurements would also lead to potential errors. Second, the protection level (PL) is evaluated. It represents the potentially largest error caused by both undetected faults and noise.

An alert limit (AL) is defined according to aviation application requirements [11]. When the estimated PL is larger than AL, an alert would be triggered and the position solution would be supposed as unavailable [12]. Integrity risk defines the probability that the actual localization error exceeds the AL, while PL is smaller than AL [11]. In such cases, the navigation system is unaware of the hazardous situation. Therefore, certifiable conditions limiting the integrity risk are stipulated to realize safety awareness.

IM for satellite navigation has been developed over decades and plays a major role in its life-critical applications [13]. Currently, the optimization-based LiDAR localization methods using low-level features, such as planar features and edge

This work was supported by the Research Centre for Data Sciences & Artificial Intelligence of The Hong Kong Polytechnic University under the project "Data-driven-assisted GNSS RTK/INS Navigation for Autonomous Systems in Urban Canyons (1-CEIR)".

Jiachen Zhang, Xikun Liu, Weisong Wen and Li-Ta. Hsu, are with The Hong Kong Polytechnic University, Hong Kong (correspondence e-mail: welson.wen@polyu.edu.hk).

This work will be submitted to the IEEE for possible publication. Copyright may be transferred without notice, after which this version may no longer be accessible. 2

features, achieve impressive performance in various scenarios [14]. LiDAR measurements are kind of similar to the GNSS ones as both of them provide range measurements. Therefore, safety-quantifiable LiDAR-based localization following a similar idea can greatly contribute to LiDAR-based autonomous driving tasks in challenging environments, e.g., driving in dense traffic involving vehicles and pedestrians, enabling safer decision-making and path planning. However, the IM technique could not directly be applied to feature-based LiDAR localization. The safety quantification of feature-based LiDAR localization is still to be investigated. Challenges on both FDE and PL estimation are delineated as follows.

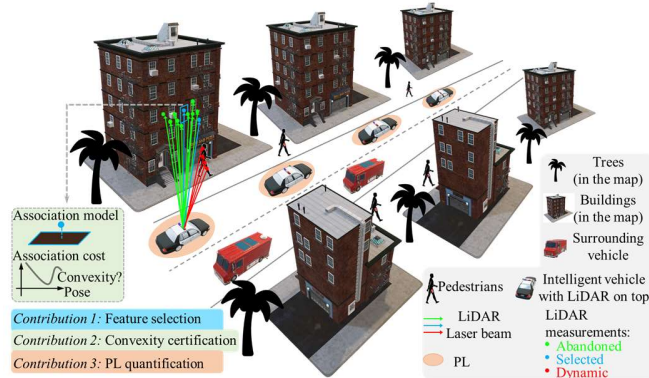


Fig. 1. Illustration of the contributions in this paper. The 3D LiDAR provides dense, omnidirectional, and stereo measurements encircling the vehicle. For clarification, only measurements in specific directions are shown by the blue, green, and red dots. The lateral and longitudinal PL is shown by the orange ellipse which defines the maximum potential error of the estimated pose.

B. Major Challenges for Safety-quantifiable LiDAR-based Localization

1) Challenges on FDE

FDE is crucial to achieving safety-quantifiable LiDAR-based localization [15]. However, it is more challenging compared with that for satellite navigation due to the two main factors.

On the one hand, at least thousands of measurements are involved for both pointwise [16] and feature-wise [17] LiDAR-based localization (while only tens in satellite navigation). FDE on such a great number has intolerable latency thus computationally intractable. Fortunately, the full measurement set provides redundant constraints. As shown in Fig. 1, the blue and green LiDAR features share similar contributions in LiDAR localization. Outlier constraints could be contained such as that on dynamic objects painted in red. Given this fact, can we select a subset of representative measurements? The computational feasibility of FDE could be guaranteed by the reduced measurements. The accuracy of the localization could be guaranteed by well-conditioned constraints. *The first challenge lies in how to select those representative measurements from the dense point clouds from 3D LiDAR.*

On the other hand, the measurement model of LiDAR is highly non-linear [17] (while that of satellite navigation could be totally tackled as a linear one after first linearization [18]). The potential faults during LiDAR localization could exist in raw LiDAR range measurements, feature extraction, point cloud registration, and convergence of the non-linear point association. All kinds of undetected faults concentratedly react to the optimization of the non-linear measurement model. The

convexity (the convex or nonconvex property) of the model determines the quality of the converged solution. In other words, the potential localization error induced by the fault existing before the optimization would be determined by the convexity of the model. As illustrated in Fig. 1, for illustration purposes, the measurement association cost is projected to one specific dimension of the pose. Its convexity in the possible pose solution space should be investigated to justify the safety quantification of LiDAR localization. In summary, *the FDE is effective only if the convex property of the LiDAR measurement model is certified. The second challenge lies in the exploration of its convexity.*

2) Challenges in PL estimation

For the safety-quantifiable LiDAR-based localization, the significant challenge consists in that the practical and applicable PL formulation has not been constructed. Besides, the numerical value of PL for the pose estimation including translation and rotation is not well developed. The PL is mainly derived and represented in the form of probability distributions for GNSS [13]. A specific numerical value of the PL would be instructive for IV. The safety could be monitored intuitively. As shown in Fig. 1, the value of PL in the lateral and the longitudinal direction is shown by the orange ellipse. It directly quantifies the potential error bounds of the pose estimations.

C. Related Works

To enable feasible FDE for LiDAR localization methods, compact and informative feature selection used for pose estimation then becomes the primary task. Feature selection methods targeting feature reduction are widely investigated in visual localization while rarely used in LiDAR localization. The work [19] drew inspiration from works [20] and [21] in the visual area. The author proposed a stochastic-greedy algorithm to select the most representative LiDAR features. The selection criterion is based on the spectral attribute of the information matrix of the LiDAR odometry. However, the impact of the feature reduction on prior map-based LiDAR localization still needs investigation.

Concerning the safety-quantification issue of LiDAR localization, the literature is sparse. The work [22] derived the integrity risk equation accounting for the feature separation degree and the incorrect feature association. However, the landmarks are assumed to be constant and repeatedly observed by each frame. While the mission-critical applications of LiDAR-based localization face a more complicated situation with landmarks coming in and out of view. The work [23] quantified the integrity risk caused by LiDAR feature association faults. All possible associations among features and prior landmarks should be evaluated which is computationally expensive. The work [24] extended the IM work [25] and [26] from GNSS to LiDAR. In detail, the feature association fault hypothesis is used to develop the probability distribution of pose estimation error and PL, which are assumed as Gaussian and chi-squared respectively. The work [27] further improved the performance of [24] in a recursive manner. Faults in a preceding time window besides that of the current epoch are considered. However, both methods supposed the measurement model is linear regardless of the realistic non-linearity of the measurement model. In addition, both methods are validated

This work will be submitted to the IEEE for possible publication. Copyright may be transferred without notice, after which this version may no longer be accessible. 3

under the simplified assumption that the associations between the features of the new coming LiDAR frame and those in the prior map are assumed known. While in realistic urban areas, the ground-true correspondence is unknown. The work [28, 29] introduced integrity monitoring for landmark-based localization in realistic applications with consideration of incorrect feature extraction and misassociations in the frame of extended Kalman filter (EKF) and particle filter, respectively. However, the landmark-based methods require typical features of the environment, such as tree trunks, light poles, etc. Safety quantification for mainstream optimization-based LiDAR localization using low-level features (e.g., planar and edge features) needs to be explored.

In summary, the existing work focuses on quantifying the impact of the feature extraction and association faults on the pose estimation error. Explicit FDE hasn't been performed. One of the common problems is that these methods are submitted to simplified assumptions thus unpractical in real urban scenes. Besides, the PL is presented in a probabilistic expression which is not instructive enough for IV. Moreover, most relevant publications aim at filter-based localization methods. To the best of our knowledge, the safety quantification method for non-linear optimization-based LiDAR localization has not been developed. The challenges exposed by safety-quantifiable LiDAR localization urgently need to be addressed.

D. Contributions

To tackle the challenges listed above, this paper proposed a safety-quantifiable planar feature-based LiDAR localization method. It's targeted at IV in realistic urban canyons with prior map requirements. It's noted that the proposed method applies to relative localization pipelines as the LiDAR is a kind of local sensor [30]. The main contributions are illustrated in Fig. 1 and summarized as follows:

(1) **Light-weight LiDAR localization with intelligent LiDAR feature selection:** The paper proposes an efficient LiDAR localization method by exploiting a small number of representative features. The spectral attributes of the information matrix provided by planar features function as the criterion of feature selection. The small quantity but well-conditioned constraints ensure accurate localization. More importantly, the efficient FDE required by safety quantification is achieved.

(2) **Certification of convex property in large pose solution space of planar feature-based LiDAR localization model:** The analytical Hessian matrix of the objective registration function relative to the pose state is rigorously derived, which is typically approximated through the Jacobian matrix and the convex property consequently is left unexplored. The positive definiteness (PD) of the Hessian matrix is further investigated from two perspectives to quantify the convexity. The certification indicates that the subsequent PL quantification is free from the problem caused by the non-convexity during the pose estimation.

(3) **Quantification of the PL for both translation and rotation estimation:** A residual-based PL quantification method is delicately designed, which is inherited from IM methods for satellite navigation [18], [31] and free from unrealistic scenario assumptions. The numerical value rather

than the possibility of the 6-degree PL of the estimated translation and rotation is calculated.

(4) **Experimental verification:** The proposed method is verified on challenging localization datasets collected from the urban canyons of Hong Kong. The feasibility of the proposed LiDAR localization and the safety quantification method is validated step-by-step.

The remainder of this paper is organized as follows. An overview of the proposed method is given in Section II. The detailed lightweight LiDAR localization method is introduced in Section III. The certification of the local convex property of the adopted LiDAR measurement model is elaborated in Section IV. In Section V, the safety quantification approaches are presented. Real-life experiments and discussions were conducted to evaluate the proposed method in Section VI. Finally, Section VII presents the conclusions and future perspectives.

II. SYSTEM OVERVIEW AND NOTATIONS

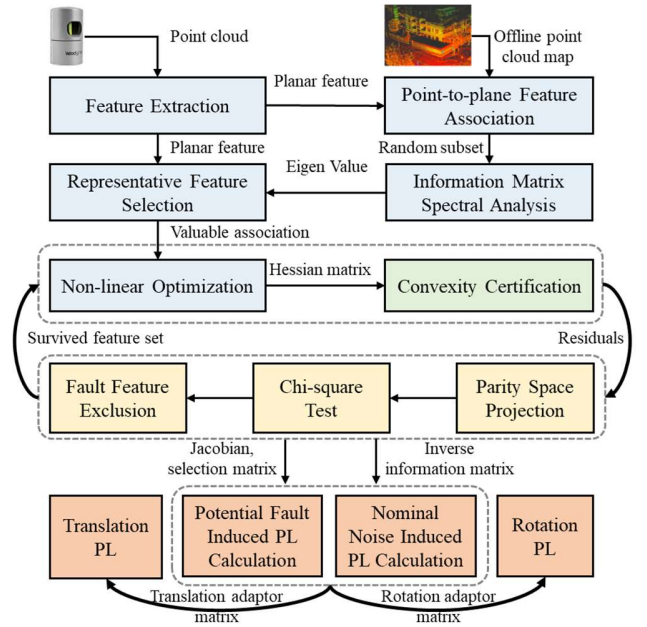


Fig. 2. Overview of the proposed method.

Fig. 2 shows an overview of the proposed method in this paper. The input of the system is the 3D point cloud generated by LiDAR. A drift-free offline point cloud map is constructed in advance. It's accumulated by registering the points with pose ground truth from NovAtel SPAN-CPT [32]. The LiDAR localization framework facilitating feasible FDE is painted in blue. Planar feature points are extracted according to the smoothness of the point [17]. Each feature is associated with a fitted local plane generated from the map. The spectral attribute of the information matrix produced by the association is investigated. Features preserving strong spectral intensity at each dimension of the pose provide well-conditioned constraints. Under the cardinality restriction, such features are iteratively selected as representative ones. Non-linear optimization is performed on the representative associations for pose estimation. The convexity of the non-linear localization model is certified based on Hessian matrix derivations.

This work will be submitted to the IEEE for possible publication. Copyright may be transferred without notice, after which this version may no longer be accessible. 4

The subsequent safety quantification is completed in two steps. At first, FDE painted in yellow is iteratively implemented. The residual vector is projected to its parity space. According to the Chi-square test in this space, the fault measurements are detected and excluded. Then, the PL calculation painted in orange is performed. The PL induced by the single potential fault fails to be detected during the FDE procedure and that induced by the noise are calculated respectively. The numerical value of the PL on each dimension of the rotation and translation is achieved with the corresponding adaptor matrix.

The safety quantification results are expected to provide a safety constraint on the pose estimation. On the one hand, the safety cost will be constructed as a residual between the pose estimation and the PL estimation. Such costs will be restricted and optimized. On the other hand, the PL will be constrained to be smaller than AL. Such formulations confirm that when minimum safety cost is achieved, the provided pose estimation has credible PL which is as tight as possible within the AL.

In this paper, matrices are denoted as bold uppercase letters, e.g. **H**. Vectors are denoted with bold lowercase letters, e.g. **p**. Variable scalars are denoted with lowercase italic letters, e.g. *t*. Constant scalars are denoted with lowercase letters, e.g. *n*. In addition, the LiDAR body frame at the *k* epoch is represented as $\{\cdot\}^{\mathcal{L}_k}$. The map frame, defined as the initial LiDAR body frame, is a kind of local world frame and is denoted as $\{\cdot\}^{\mathcal{M}}$.

III. LIGHTWEIGHT LiDAR LOCALIZATION WITH INTELLIGENT FEATURE SELECTION

The lightweight planar feature-based LiDAR localization method contributed by the intelligent representative feature selection is elaborated in this part.

A. Planar Feature-based LiDAR Localization Formulation

This section provides a brief description of the planar feature-based LiDAR localization formulation used in this paper.

Referred to [17], planar feature points are first extracted according to the horizontal smoothness. LiDAR localization is further accomplished via the registration between the planar feature points in the current frame and the prior map. Specifically, the registration is formulated as a non-linear optimization problem. As depicted in Fig. 3, the one-shot optimization manner is adopted so that the state of each epoch is independently estimated. The objective function is defined as follows,

$$\mathbf{T}_{\mathcal{L}_k}^{\mathcal{M}} = \underset{\mathbf{T}_{\mathcal{L}_k}^{\mathcal{M}}}{\operatorname{argmin}} f(\mathbf{T}_{\mathcal{L}_k}^{\mathcal{M}}) \quad (1)$$

$$\text{with } f(\mathbf{T}_{\mathcal{L}_k}^{\mathcal{M}}) = \frac{1}{2} \sum_{i=1}^m r_{k,i}^T \mathbf{w}_{k,i} r_{k,i},$$

where the pose of the *k*-th LiDAR frame to be estimated relative to the prior map is denoted as $\mathbf{T}_{\mathcal{L}_k}^{\mathcal{M}} = \begin{bmatrix} \mathbf{R}_{\mathcal{L}_k}^{\mathcal{M}} & \mathbf{t}_{\mathcal{L}_k}^{\mathcal{M}} \\ \mathbf{0}_{1 \times 3} & 1 \end{bmatrix} \in SE(3)$ containing the rotation part $\mathbf{R}_{\mathcal{L}_k}^{\mathcal{M}} \in SO(3)$ and the translation part $\mathbf{t}_{\mathcal{L}_k}^{\mathcal{M}} \in \mathbb{R}^3$ [33]. For simplicity, the rotation could also be expressed as its corresponding Lie algebra $\boldsymbol{\phi}_{\mathcal{L}_k}^{\mathcal{M}} \in SO(3)$ [34]. The initial guess of the pose is predicted under the assumption of uniform motion as follows:

$$\tilde{\mathbf{T}}_{\mathcal{L}_k}^{\mathcal{M}} = \mathbf{T}_{\mathcal{L}_{k-1}}^{\mathcal{M}} (\mathbf{T}_{\mathcal{L}_{k-2}}^{\mathcal{M}})^{-1} \mathbf{T}_{\mathcal{L}_{k-1}}^{\mathcal{M}}. \quad (2)$$

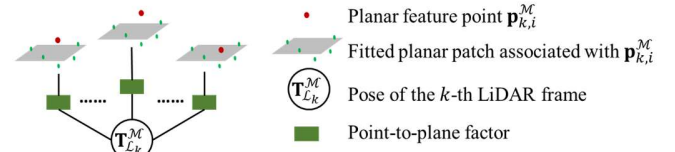


Fig. 3. Illustration of the proposed planar feature-based LiDAR localization method.

The *i*-th planar feature registration residual constraining the *k*-th pose is denoted as $r_{k,i}$ in (1). Planar feature point sets in the *k*-th LiDAR frame and the prior map are denoted as $\mathcal{P}^{\mathcal{L}_k}$ and $\mathcal{P}^{\mathcal{M}}$ respectively. For feasible FDE, a subset of representative features denoted as $\mathcal{F}^{\mathcal{L}_k}$ is selected from $\mathcal{P}^{\mathcal{L}_k}$ to perform the registration. The selection approach will be detailed in section III.B. The *i*-th point among the *m* selected planar points $\mathbf{p}_i^{\mathcal{L}_k} \in \mathcal{F}^{\mathcal{L}_k}$ with $i \in [1, m]$, is projected to the $\mathcal{P}^{\mathcal{M}}$ denoted as $\mathbf{p}_{k,i}^{\mathcal{M}}$ under the initial guess. As shown in Fig. 3, in $\mathcal{P}^{\mathcal{M}}$ a planar patch painted in gray, which $\mathbf{p}_{k,i}^{\mathcal{M}}$ is expected to be associated with, could be parameterized depending on the principal component analysis (PCA) of neighbors around $\mathbf{p}_{k,i}^{\mathcal{M}}$ [35]. The residual namely the distance between $\mathbf{p}_i^{\mathcal{L}_k}$ and the fitted planar patch is the function of $\mathbf{T}_{\mathcal{L}_k}^{\mathcal{M}}$ as follows,

$$r_{k,i} = \mathbf{n}_{k,i}^T \mathbf{p}_{k,i}^{\mathcal{M}} + d_{k,i} \quad (3)$$

with $\mathbf{p}_{k,i}^{\mathcal{M}} = \mathbf{T}_{\mathcal{L}_k}^{\mathcal{M}} \mathbf{p}_i^{\mathcal{L}_k}$,

where $\mathbf{n}_{k,i}$ and $d_{k,i}$ are the normal vector and the constant parameter of the planar patch respectively.

The weight accounting for the uncertainty of the residual is denoted as $\mathbf{w}_{k,i}$ in (1), which is empirically determined. It's interpreted as a constant which is the inverse of the covariance of the nominal Gaussian noise in the LiDAR raw measurements.

Typical second-order gradient-based non-linear optimization algorithm Levenberg-Marquardt (LM) [36] implemented in Ceres Solver [37] is utilized to solve the objective function. During optimization, the following linearization definitions hold by stacking the residuals in the matrix form:

$$\mathbf{r}_k = \mathbf{J}_k \mathbf{x}_k + \mathbf{b}_k + \boldsymbol{\eta}_k \quad (4)$$

with $\mathbf{r}_k = \begin{bmatrix} r_1 \\ r_2 \\ \vdots \\ r_m \end{bmatrix}$, $\mathbf{x}_k = \begin{bmatrix} \boldsymbol{\phi}_{\mathcal{L}_k}^{\mathcal{M}} \\ \mathbf{t}_{\mathcal{L}_k}^{\mathcal{M}} \end{bmatrix} \in \mathbb{R}^6$, $\mathbf{J}_k = \frac{\partial \mathbf{r}_k}{\partial \mathbf{x}_k^T}$,

where \mathbf{x}_k is the pose to be estimated equally to $\mathbf{T}_{\mathcal{L}_k}^{\mathcal{M}}$. $\mathbf{J}_k \in \mathbb{R}^{m \times 6}$ denotes the Jacobian matrix of \mathbf{r}_k relative to \mathbf{x}_k which could be found in [30]. The *i*-th row of \mathbf{J}_k is the Jacobian matrix of r_i relative to \mathbf{x}_k denoted as $\mathbf{J}_{k,i} \in \mathbb{R}^{1 \times 6}$. The residuals led by bias from faulty measurements is denoted as $\mathbf{b}_k \in \mathbb{R}^m$. The residuals are also disturbed by Gaussian noise $\boldsymbol{\eta}_k \in \mathbb{R}^m$ with $\boldsymbol{\eta}_k \sim \mathcal{N}(\mathbf{0}, \mathbf{Q}_k)$. \mathbf{Q}_k is empirically determined according to the precision of LiDAR measurements. The weight matrix \mathbf{W}_k for \mathbf{r}_k is denoted as:

$$\mathbf{W}_k = \mathbf{Q}_k^{-1} = \begin{bmatrix} \mathbf{w}_{k,1} & 0 & \cdots & 0 \\ 0 & \mathbf{w}_{k,2} & \cdots & 0 \\ \vdots & \vdots & \ddots & \vdots \\ 0 & 0 & \cdots & \mathbf{w}_{k,m} \end{bmatrix} \in \mathbb{R}^{m \times m}. \quad (5)$$

Moreover, the quantified effect of different \mathbf{W}_k on the PL is fully investigated in the experiments.

This work will be submitted to the IEEE for possible publication. Copyright may be transferred without notice, after which this version may no longer be accessible. 5

B. Representative Feature Selection Based on Information Matrix Spectrum Analysis

In this section, the representative feature selection approach involved in pose estimation is presented, which aims to achieve both efficient FDE for safety quantification and highly accurate pose estimation.

The information matrix contributed by each feature for the estimated pose is defined as $\mathbf{\Gamma}_{k,i} = \mathbf{J}_{k,i}^T \mathbf{w}_{k,i} \mathbf{J}_{k,i}$ [38]. The spectral attribute of $\mathbf{\Gamma}_{k,i}$ measures the quality of the constraint on the estimated pose [39]. The eigenvalues are exploited to reveal the spectral attribute of a matrix in this paper [21], [39]. Each of the six eigenvalues of the information matrix reflects the spectral intensity in the corresponding dimension of the translation and rotation. A large eigenvalue reflects the strong spectral intensity and thus provides a strong and healthy constraint. On the contrary, a small eigenvalue reflecting weak spectral intensity provides a weak or even ill constraint. It's generally accepted that more features involved would achieve information matrices with stronger spectral attributes in all dimensions. The localization methods tend to use all the available features. However, the great number of features make the FDE procedure for safety quantification intractable. Fortunately, the spectrum gains of the information matrices are demonstrated to be monotone and submodular [40]. The subset of features named representative features, which guarantees a strong spectrum intensity of the information matrices, could be achieved. Most importantly, the cardinality restriction of the subset promises efficient FDE for safety quantification.

Algorithm 1 Representative Feature Selection.

Inputs: Full feature set $\mathcal{P}^{\mathcal{L}_k}$, cardinality restriction on representative feature set m , the initial guess of the pose $\tilde{\mathbf{T}}_{\mathcal{L}_k}^{\mathcal{M}}$.

Outputs: Representative feature set $\mathcal{F}^{\mathcal{L}_k}$.

$\mathcal{F}^{\mathcal{L}_k} \leftarrow \emptyset$.

While $|\mathcal{F}^{\mathcal{L}_k}| < m$,

Produce the subset $\mathcal{S}^{\mathcal{L}_k}$ by random sampling from $\mathcal{P}^{\mathcal{L}_k}$.

Define minimum spectrum intensity (MEV) set $e^{\mathcal{S}^{\mathcal{L}_k}}$ for $\mathcal{S}^{\mathcal{L}_k}$.

$e^{\mathcal{S}^{\mathcal{L}_k}} \leftarrow \emptyset$.

For each $\mathbf{p}_i^{\mathcal{L}_k} \in \mathcal{S}^{\mathcal{L}_k}$,

Calculate the registration residual and the information matrix:

$$\mathbf{p}_{k,i}^{\mathcal{M}} = \tilde{\mathbf{T}}_{\mathcal{L}_k}^{\mathcal{M}} \mathbf{p}_i^{\mathcal{L}_k},$$

$$r_i = \mathbf{n}_i^T \mathbf{p}_{k,i}^{\mathcal{M}} + d_i,$$

$$\mathbf{\Gamma}_{k,i} = \mathbf{J}_{k,i}^T \mathbf{w}_{k,i} \mathbf{J}_{k,i}.$$

Calculate the MEV $e_{\min,i}$ of $\mathbf{\Gamma}_{k,i}$.

$$e^{\mathcal{S}^{\mathcal{L}_k}} \leftarrow e^{\mathcal{S}^{\mathcal{L}_k}} \cup e_{\min,i}$$

End for.

$$i \leftarrow \underset{i}{\operatorname{argmax}} e^{\mathcal{S}^{\mathcal{L}_k}}.$$

$$\mathcal{F}^{\mathcal{L}_k} \leftarrow \mathcal{F}^{\mathcal{L}_k} \cup \mathbf{p}_i^{\mathcal{L}_k}, \mathcal{P}^{\mathcal{L}_k} \leftarrow \mathcal{P}^{\mathcal{L}_k} \setminus \mathbf{p}_i^{\mathcal{L}_k}$$

End while.

The representative feature selection issue is formulated as follows:

$$\underset{\mathcal{F}^{\mathcal{L}_k} \subseteq \mathcal{P}^{\mathcal{L}_k}}{\operatorname{argmax}} e(\mathcal{F}^{\mathcal{L}_k}) \quad (6)$$

$$\text{with } e(\mathcal{F}^{\mathcal{L}_k}) = \sum_{i=1}^m e_{\min,i} \text{ and } |\mathcal{F}^{\mathcal{L}_k}| \leq m,$$

where $e_{\min,i}$ represents the minimum eigenvalue (MEV) of the information matrix $\mathbf{\Gamma}_{k,i}$. The cardinality restriction is defined as $|\mathcal{F}^{\mathcal{L}_k}| \leq m$. The selected feature number is limited by m which is empirically set as 20% of all the available features [21]. To construct $\mathcal{F}^{\mathcal{L}_k}$, the features maximizing the minimum spectrum intensity sum of the information matrices should be iteratively selected from the full feature set $\mathcal{P}^{\mathcal{L}_k}$. Inspired by the work [40] and [19], each representative feature is searched on a random subset of $\mathcal{P}^{\mathcal{L}_k}$ instead of the whole $\mathcal{P}^{\mathcal{L}_k}$. Otherwise, there would be intolerable time consumption. The detailed procedure of the representative feature selection is delineated in Algorithm 1.

IV. CONVEX PROPERTY CERTIFICATION OF THE LIDAR LOCALIZATION MODEL

This section elaborates on the convex property certification of the localization model defined by (1), including Hessian matrix derivation and its two-perspective PD investigation. Such certification ensures that the PL resulting from the undetected faults and noise in the non-linear localization model is credibly assessed. There won't be interference from the convergence quality caused by the non-convexity.

A. Convexity Certification Preparation: Analytical Hessian Matrix Derivation

Above all, the definiteness (e.g. PD, negative definiteness, etc.) of the Hessian matrix at the final converged pose solution determines the local convexity (e.g. convex property, concave property, etc.) of the objective function [41]. To be specific, the PD indicates the strictly local convex property at the converged solution. Therefore, it's in expectation as it guarantees that at least local optimum is achieved given the initial guess. Furthermore, for the commonly used second-order gradient-based non-linear optimization algorithms such as the L-M algorithm used in this paper, the PD of the Hessian matrix at the operating point before convergence is expected. It essentially provides another perspective of the local convex property of the localization model at the converged state. It implies that the optimization is iterated toward the descending direction of the objective function [41]. The solution is updated in line with the least-square goal.

Specifically, the Hessian matrix of the objective function defined by (1) relative to the pose state is derived based-on matrix differential on Euclidean space and manifolds, which can be derived as

$$\mathbf{H}_k = \frac{\partial f(\mathbf{x}_k)}{\partial \mathbf{x}_k \partial \mathbf{x}_k^T}. \quad (7)$$

Substituting the $\mathbf{f}(\cdot)$ defined as (1), \mathbf{H}_k could be further factorized as

$$\mathbf{H}_k = \sum_{i=1}^m \mathbf{H}_{k,i} \quad (8)$$

$$\text{with } \mathbf{H}_{k,i} = \frac{\partial f_i(\mathbf{x}_k)}{\partial \mathbf{x}_k \partial \mathbf{x}_k^T} \text{ and } f_i(\mathbf{x}_k) = \frac{1}{2} r_{k,i}^T \mathbf{w}_{k,i} r_{k,i},$$

The chain rule is exploited to derive $\mathbf{H}_{k,i}$. $\mathbf{p}_{k,i}^{\mathcal{M}}$ is selected as the intermediate variable according to (3). Referring to $\mathbf{p}_{k,i}^{\mathcal{M}}$, $f_i(\mathbf{x}_k)$ is expanded according to the second-order Taylor approximation as

This work will be submitted to the IEEE for possible publication. Copyright may be transferred without notice, after which this version may no longer be accessible. 6

$$f_i(\mathbf{p}_{k,i}^{\mathcal{M}} + \delta \mathbf{p}_{k,i}^{\mathcal{M}}) = f_i(\mathbf{p}_{k,i}^{\mathcal{M}}) + (\mathbf{G}_{\mathbf{p}^{\mathcal{M}}}^f)^T \delta \mathbf{p}_{k,i}^{\mathcal{M}} + \frac{1}{2} (\delta \mathbf{p}_{k,i}^{\mathcal{M}})^T (\mathbf{H}_{\mathbf{p}^{\mathcal{M}}}^f) (\delta \mathbf{p}_{k,i}^{\mathcal{M}}), \quad (9)$$

where the gradient matrix and the Hessian matrix are denoted as $\mathbf{G}_{\mathbf{p}^{\mathcal{M}}}^f$ and $\mathbf{H}_{\mathbf{p}^{\mathcal{M}}}^f$ respectively. The detailed derivation of these two matrices can be found in Appendix A. The increment $\delta \mathbf{p}_{k,i}^{\mathcal{M}}$ is induced by the increment $\delta \mathbf{x}_k$ as follows,

$$\delta \mathbf{p}_{k,i}^{\mathcal{M}} = \mathbf{D}_{\mathbf{x}}^{\mathbf{p}^{\mathcal{M}}} \delta \mathbf{x}_k, \quad (10)$$

in which $\mathbf{D}_{\mathbf{x}}^{\mathbf{p}^{\mathcal{M}}}$ represents the Jacobian matrix of $\mathbf{p}_{k,i}^{\mathcal{M}}$ relative to \mathbf{x}_k . The detailed derivation can be found in Appendix B. Replacing $\delta \mathbf{p}_{k,i}^{\mathcal{M}}$ in (9), the second-order Taylor approximation of $f_i(\mathbf{x}_k)$ referring to \mathbf{x}_k is finally derived as follows,

$$f_i(\mathbf{x}_k + \delta \mathbf{x}_k) = f_i(\mathbf{x}_k) + (\mathbf{G}_{\mathbf{x}}^f)^T \mathbf{D}_{\mathbf{x}}^{\mathbf{p}^{\mathcal{M}}} \delta \mathbf{x}_k + \frac{1}{2} \delta \mathbf{x}_k^T \left((\mathbf{D}_{\mathbf{x}}^{\mathbf{p}^{\mathcal{M}}})^T \mathbf{H}_{\mathbf{p}^{\mathcal{M}}}^f \mathbf{D}_{\mathbf{x}}^{\mathbf{p}^{\mathcal{M}}} \right) \delta \mathbf{x}_k, \quad (11)$$

where the Hessian matrix of $f_i(\mathbf{x}_k)$ referring to \mathbf{x}_k namely $\mathbf{H}_{k,i}$ is represented as

$$\mathbf{H}_{k,i} = (\mathbf{D}_{\mathbf{x}}^{\mathbf{p}^{\mathcal{M}}})^T \mathbf{H}_{\mathbf{p}^{\mathcal{M}}}^f \mathbf{D}_{\mathbf{x}}^{\mathbf{p}^{\mathcal{M}}}. \quad (12)$$

Analytical expression of \mathbf{H}_k is finally achieved by adding all $\mathbf{H}_{k,i}$ as shown in (12). In Section VI, to certify the convexity of the objective function, the eigen decomposition of the Hessian matrix is performed and the decomposed information is investigated.

B. Dual-perspective Convexity Certification Approach

The pose solutions around the initial guess and the converged pose comprise the possible pose solution space. The investigation of the convexity of the non-linear LiDAR localization model should be performed in this space. This section provides a dual-perspective approach to quantify convexity.

On the one hand, the definiteness of the Hessian matrix at the converged pose solution is investigated given different initial guesses. Besides the initial guesses derived from the uniform motion assumption, other guesses are produced by adding increments to it. If the same converged pose and its PD could be maintained along with the variation of the initial guess, the convex property is proved in the possible solution space. On the other hand, given the specific initial guess derived from the uniform motion assumption, the definiteness of the Hessian matrix around the converged pose is investigated. If the PD could be maintained, the objective function is in the descending direction from the neighbors of the converged pose to the converged pose itself. In other words, the converged pose is the one with the minimal cost in the surrounding solution space. Then the convex property is dually demonstrated.

V. SAFETY QUANTIFICATION FOR PLANAR FEATURE-BASED LIDAR LOCALIZATION

The safety quantification of the planar feature-based LiDAR localization results is inspired by the residual-based receiver autonomous integrity monitoring (RAIM) method for GNSS [18], [31]. Authoritative AL for IV hasn't been developed by

related organizations. Therefore, the integrity risk couldn't be quantified. This paper implements safety quantification in the manner of calculating the numerical value of PL on each dimension of the pose. As mentioned before, it's more instructive and intuitionistic for IV.

Algorithm 2 Iterative Faulty Measurements Detection and Exclusion on Parity Space

Inputs: The original representative planar feature set $\mathcal{F}^{\mathcal{L}_k}$ with size m at time epoch k . The prior planar feature map $\mathcal{P}^{\mathcal{M}}$. The initial guess of the pose $\hat{\mathbf{T}}_{\mathcal{L}_k}^{\mathcal{M}}$. Significance level α for Chi-square test.

Outputs: The fault-excluded planar feature set $\bar{\mathcal{F}}^{\mathcal{L}_k}$ and the optimized pose $\hat{\mathbf{T}}_{\mathcal{L}_k}^{\mathcal{M}}$ at time epoch k .

Step 1: Register $\mathcal{F}^{\mathcal{L}_k}$ to $\mathcal{P}^{\mathcal{M}}$ achieving converged $\hat{\mathbf{T}}_{\mathcal{L}_k}^{\mathcal{M}}$ and \mathbf{r}_k .

Step 2: Project \mathbf{r}_k to its parity space as $\mathbf{p}_k = \mathbf{U}_k \mathbf{r}_k = [p_1, p_2, \dots, p_m]^T$.

Step 3: Perform the Chi-square test on the statistic $\lambda_k = \bar{\mathbf{p}}_k^T \bar{\mathbf{p}}_k$ given the critical value $\varepsilon = \chi_{m-6,1-\alpha}^2$.

If $\lambda_k > \varepsilon$,

$$\mathbf{p}_j^{\mathcal{L}_k} = \underset{\mathbf{p}_j^{\mathcal{L}_k}}{\operatorname{argmax}} \lambda_k, \mathbf{p}_j^{\mathcal{L}_k} \in \mathcal{F}^{\mathcal{L}_k}.$$

$$\bar{\mathcal{F}}^{\mathcal{L}_k} \leftarrow \mathcal{F}^{\mathcal{L}_k} \setminus \mathbf{p}_j^{\mathcal{L}_k}.$$

$$m \leftarrow m - 1, \varepsilon \leftarrow \chi_{m-6,1-\alpha}, \mathcal{F}^{\mathcal{L}_k} \leftarrow \bar{\mathcal{F}}^{\mathcal{L}_k}.$$

Repeat steps from 1 to 3.

Else,

Return $\bar{\mathcal{F}}^{\mathcal{L}_k}$ and $\hat{\mathbf{T}}_{\mathcal{L}_k}^{\mathcal{M}}$.

A. Fault Detection and Exclusion

In this section, the FDE method preparing for PL calculation is presented.

The parity space approach to reject faulty measurements has been developed for decades in the control field [42]. The parity space is a kind of measurement space independent from the state. The rejection is performed in this space where the isolation from the state enhances the sensitivity of the measurement model to the fault.

The first key point of the approach consists of parity space construction. The projection matrix \mathbf{U}_k is defined to project the residual vector \mathbf{r}_k to its parity space denoted as \mathbf{p}_k . \mathbf{U}_k is demonstrated as (7) in [42] to be in the null space of the linearized coefficient matrix of the measurement model as follows,

$$\mathbf{U}_k \mathbf{J}_k = \mathbf{0}. \quad (13)$$

Adequate \mathbf{U}_k is specified as

$$\mathbf{U}_k = \mathbf{I} - \mathbf{J}_k (\mathbf{J}_k^T \mathbf{W}_k \mathbf{J}_k)^{-1} \mathbf{J}_k^T \mathbf{W}_k. \quad (14)$$

Then, the \mathbf{p}_k is achieved as

$$\mathbf{p}_k = \mathbf{U}_k \mathbf{r}_k = \mathbf{U}_k \mathbf{b}_k + \mathbf{U}_k \boldsymbol{\eta}_k. \quad (15)$$

where $\mathbf{p}_k \sim \mathcal{N}(\boldsymbol{\mu}_k, \mathbf{U}_k \mathbf{Q}_k \mathbf{U}_k^T)$ according to the linear transformation of the Gaussian distribution. With no faulty measurements, $\boldsymbol{\mu}_k$ is the zero vector as the $\boldsymbol{\eta}_k$ follows the zero mean Gaussian distribution. While with faulty measurements involved, $\boldsymbol{\mu}_k$ is decided by $\mathbf{U}_k \mathbf{b}_k$ which is significantly larger. The standardized \mathbf{p}_k is denoted as $\bar{\mathbf{p}}_k$. The quadratic sum of $\bar{\mathbf{p}}_k$ subjects to Chi-square distribution represented as $\lambda_k = \bar{\mathbf{p}}_k^T \bar{\mathbf{p}}_k$.

This work will be submitted to the IEEE for possible publication. Copyright may be transferred without notice, after which this version may no longer be accessible. 7

and $\lambda_k \sim \chi_{m-6}^2$. For given significance level α , the corresponding critical value $\chi_{m-6,1-\alpha}^2$ denoted as ε is determined. Consequently, the faulty measurements could be detected through a comparison between the λ_k and ε , which is the Chi-square test. It's concluded that if λ_k is larger than ε , faulty measurements occur.

Once faulty measurements are detected, the feature that contributes most to λ_k is removed and the optimization is implemented on the remained feature sets. The process is repeated until the Chi-square test on λ_k is passed which means no fault exists anymore. The detail is shown in Algorithm 2.

B. Residual-Based Translation and Rotation PL Calculation

This section presents the calculation of PL which can be formulated as follows [43],

$$\mathbf{\Omega}_k = \mathbf{\Omega}_{k,b} + \mathbf{\Omega}_{k,\eta}, \quad (16)$$

where $\mathbf{\Omega}_k \in \mathbb{R}^6$ is the PL for the 6D pose estimation. $\mathbf{\Omega}_{k,b} \in \mathbb{R}^6$ and $\mathbf{\Omega}_{k,\eta} \in \mathbb{R}^6$ represent the part induced by undetected fault and the Gaussian noise respectively.

The $\mathbf{\Omega}_{k,\eta}$ is the commonly used "3-sigma" that is the triple standard deviation of the error in the estimated pose resulting from the Gaussian noise denoted as $\boldsymbol{\eta}_k$ in (4). It's defined as

$$\mathbf{\Omega}_{k,\eta} = 3\sqrt{\text{diag}((\mathbf{J}_k^T \mathbf{W}_k \mathbf{J}_k)^{-1})}, \quad (17)$$

where $\text{diag}(\cdot)$ denotes the diagonal elements of (\cdot) . The detailed derivation of $\mathbf{\Omega}_{k,\eta}$ could be found in Appendix C. The remained section focuses on the derivation of $\mathbf{\Omega}_{k,b}$.

Considering the residual \mathbf{b}_k induced by the faulty measurements, its impact on the pose estimation is quantified as

$$\delta \mathbf{x}_k = (\mathbf{J}_k^T \mathbf{W}_k \mathbf{J}_k)^{-1} \mathbf{J}_k^T \mathbf{W}_k \mathbf{b}_k, \quad (18)$$

which is derived from the linearized measurement model shown in (4). The factorization of $\delta \mathbf{x}_k$ on each component of the pose is as follows,

$$\omega_{k,b,c}^2 = \delta \mathbf{x}_k^T \mathbf{C}_c \delta \mathbf{x}_k = \mathbf{b}_k^T \boldsymbol{\Sigma}_{k,c} \mathbf{b}_k \quad (19)$$

$$\text{with } \boldsymbol{\Sigma}_{k,c} = \mathbf{W}_k \mathbf{J}_k (\mathbf{J}_k^T \mathbf{W}_k \mathbf{J}_k)^{-1} \mathbf{C}_c (\mathbf{J}_k^T \mathbf{W}_k \mathbf{J}_k)^{-1} \mathbf{J}_k^T \mathbf{W}_k,$$

where the subscript c represents the index of the pose component arranged in \mathbf{x}_k . It ranges from 1 to 6 and corresponds to the rotation and translation on the x-axis, y-axis, and z-axis respectively. $\omega_{k,b,c}$ represents the c -th component of $\mathbf{\Omega}_{k,b}$. \mathbf{C}_c is the dimension adaptor matrix for component selection with c -th diagonal element assigned 1 and all the others 0. For instance, the adaptor matrix for the rotation on the z-axis is defined as

$$\mathbf{C}_3 = \begin{bmatrix} 0 & 0 & 0 & 0 & 0 & 0 \\ 0 & 0 & 0 & 0 & 0 & 0 \\ 0 & 0 & 1 & 0 & 0 & 0 \\ 0 & 0 & 0 & 0 & 0 & 0 \\ 0 & 0 & 0 & 0 & 0 & 0 \\ 0 & 0 & 0 & 0 & 0 & 0 \end{bmatrix}. \quad (20)$$

Moreover, the c -th component of $\mathbf{\Omega}_{k,b}$ is defined as

$$\tilde{\omega}_{k,b,c} = \underset{\mathbf{b}_k}{\text{argmax}} \omega_{k,b,c}. \quad (21)$$

Considering the chi-square test elaborated in Algorithm 2, the constraint on \mathbf{b}_k holds as follows,

$$\mathbf{b}_k^T \boldsymbol{\Lambda}_k \mathbf{b}_k \leq \varepsilon, \quad (22)$$

where $\boldsymbol{\Lambda}_k = \mathbf{W}_k \mathbf{U}_k$. As demonstrated in [31], under this constraint, $\mathbf{\Omega}_{k,b}$ is further derived with $\tilde{\omega}_{k,b,c}$ defined as follows,

$$\tilde{\omega}_{k,b,c}^2 = \underset{\mathbf{y}_k}{\text{argmax}} \{ \max \langle \boldsymbol{\Sigma}_{k,c}, \mathbf{y}_k, \boldsymbol{\Lambda}_k \rangle_{\text{EV}} \}, \quad (23)$$

where $\mathbf{y}_k \in \mathbb{R}^m$ denotes the binary vector for undetected faulty measurement selection. For example, if the third planar feature in $\bar{\mathcal{F}}^{\mathcal{L}_k}$ is assumed the potential fault after FDE, the third element of \mathbf{y}_k is assigned as 1 while others are 0 as follows,

$$\mathbf{y}_k = [0 \ 0 \ 1 \ 0 \ \cdots \ 0]^T. \quad (24)$$

One fault hypothesis is adopted in this paper for pilot validation of the proposed formulation. The formulation could be extended to that with multiple undetected faults hypothesis in compromise of computational complexity.

In (23), $\max \langle \boldsymbol{\Sigma}_{k,c}, \mathbf{y}_k, \boldsymbol{\Lambda}_k \rangle_{\text{EV}}$ is defined as the maximum eigenvalue of $\mathbf{y}_k^T \boldsymbol{\Sigma}_{k,c} \mathbf{y}_k (\mathbf{y}_k^T \boldsymbol{\Lambda}_k \mathbf{y}_k)^{-1}$. All the m possible \mathbf{y}_k are enumerated to find the $\tilde{\omega}_{k,b,c}$.

In summary, according to the (16), (17), and (23), the PL on the c -th component of the 6D pose is denoted as $\omega_{k,c}$ and expressed as

$$\omega_{k,c} = \tilde{\omega}_{k,b,c} + \mathbf{\Omega}_{k,\eta,c}, \quad (25)$$

where $\mathbf{\Omega}_{k,\eta,c}$ is the c -th element of $\mathbf{\Omega}_{k,\eta}$.

VI. EXPERIMENT RESULTS AND DISCUSSION

A. Introduction of the Experiment

Experimental scenes: The proposed safety-quantifiable planar feature-based LiDAR localization method is verified on two typical urban canyons in Hong Kong. The first one is denoted as urban canyon 1, which is located in the light-urbanized area of Kowloon Tong. The data lasts for around 200 seconds, the total length of the trajectory is around 680 meters. As shown in Fig. 4, the buildings are relatively low with less traffic density. The second one is denoted as urban canyon 2. It's located in the more urbanized area of Tsim Sha Tsui and open-sourced in our UrbanNav dataset [32]. The scene is complicated with high-building groups and various transportation participants. The data of urban canyons 2 lasts longer for around 400 seconds with the total length of the trajectory around 1840 meters.

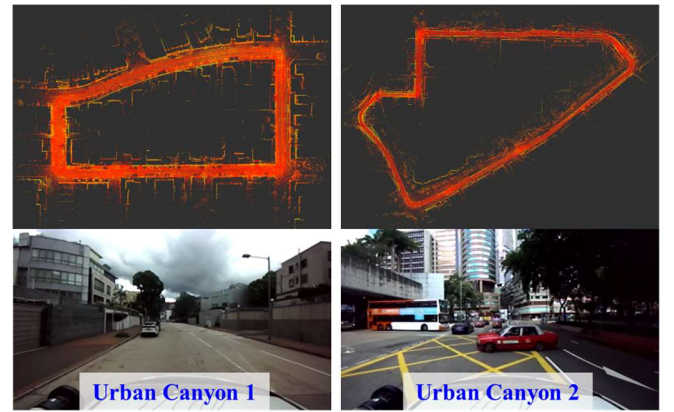


Fig. 4. The prior point cloud map (top) and typical scene (bottom) of the evaluated urban canyons 1 and 2.

This work will be submitted to the IEEE for possible publication. Copyright may be transferred without notice, after which this version may no longer be accessible. 8

Sensor setups: The installation details of the data collection vehicle can be found in our open-sourced UrbanNav dataset [32]. In both experiments, the Velodyne HDL-32E, a 32-channel mechanical 3D LiDAR, is exploited to produce point clouds at a frequency of 10 Hz. The NovAtel SPAN-CPT, a GNSS (GPS, GLONASS, and Beidou) RTK/INS (fiber-optic gyroscopes) integrated navigation system was used to provide the ground truth of pose estimation at a frequency of 100 Hz. The transformation matrix between the two sensors has been calibrated beforehand. The LiDAR point cloud is collected via the robot operation system (ROS) [44]. Thus, time synchronization is implemented under Unix time.

In the experiment, we use the real-time 10 Hz point cloud observation from the LiDAR as the input cloud. In the meantime, the point cloud of each frame is registered to the global frame according to the ground truth and then accumulated to produce the offline point cloud map. The accumulated offline point cloud maps for urban canyons 1 and 2 are depicted in Fig. 4.

The coordinate axis x , y , z of the LiDAR body frame point to the right (lateral), forward (longitudinal), and up of the vehicle respectively. The z -axis is defined as the vertical direction of the LiDAR body. The orientation is defined as the rotation around the z -axis quantitatively and depicted as the positive y direction in figures. The plane constructed by the x -axis and the y -axis is defined as the horizontal direction of the LiDAR body.

Experimental contents: To demonstrate the main contributions of this paper, we evaluate the performance of the proposed method in the following aspects:

(a) **Pose estimation accuracy:** To verify the effectiveness of the proposed FDE-feasible LiDAR localization framework, the accuracy performances with different cardinality restrictions of representative feature selection are investigated.

The proposed pipeline was developed referring to F-LOAM [30] which is one of state of the art (SOTA) LiDAR localization methods. We adapted F-LOAM with the proposed intelligent representative feature selection method. Thus, the proposed localization pipeline exploiting 100% available features is the SOTA conventional feature-based LiDAR localization method.

Due to the offline map referenced, the absolute pose error (APE) including the absolute translation error (ATE) and the absolute rotation error (ARE) implemented in EVO [45] is adopted as the accuracy metric.

(b) **Convex property certification for the pose estimation model:** To quantify the convexity of the localization model, the convex property under different initial guesses and that around the converged pose is extensively analyzed.

(c) **PL quantification for both translation and rotation estimation:** The PL calculation results on 6d pose components are compared with the “3-sigma” pose estimation error from Gaussian noise (conventional safety-quantification results) and the practical pose estimation error namely APE.

B. Experimental Results in Urban Canyon 1

1) Pose Estimation Accuracy in Urban Canyon 1

Fig. 5 illustrates the root mean squared (RMS) ATE of pose estimations from the proposed FDE-feasible LiDAR localization framework. The horizontal axis represents different cardinality restrictions for representative feature selection. It's denoted by feature percentage, which is defined as the selected feature number m mentioned in Algorithm 1 divided into the total available feature number. With the feature percentage set to 6%, the largest RMS ATE of 0.272 m is achieved. As the feature percentage increased to 20%, the RMS ATE decreased significantly by 44% to 0.152 m. However, with more features ($> 20\%$) involved, the accuracy performance of the translation estimation maintains the same level. When all the available features are exploited for the localization (conventional SOTA method), the RMS ATE is slightly improved by 2.6% to 0.148 m compared with that when only 20% representative features are selected to use.

Fig. 6 illustrates the RMS ARE of the proposed FDE-feasible LiDAR localization framework given different feature percentages. The RMS ARE was continuously decreased by 74% from 1.027 degrees to 0.269 degrees as the feature percentage increased from 6% to 20%. After this, minor ARE improvement is achieved as the feature percentage is further increased.

In summary, the monotonicity and sub-modularity of the spectrum gains of the information matrix concerning the feature number during the translation and rotation estimation are exhibited in Fig. 5 and Fig. 6 respectively. The result indicates that when 20% of representative features are exploited, comparable translation and rotation estimation accuracy is achieved compared to the conventional SOTA method that uses all the features. Therefore, the effectiveness of the proposed representative feature selection method is verified. This method, aiming at feasible FDE for the safety-aware LiDAR localization pipeline, in the meanwhile guarantees accurate performance.

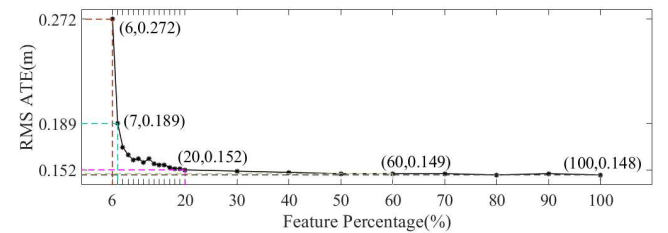


Fig. 5. RMS ATE produced by the proposed FDE-feasible LiDAR localization framework with varying feature percentages in urban canyon 1

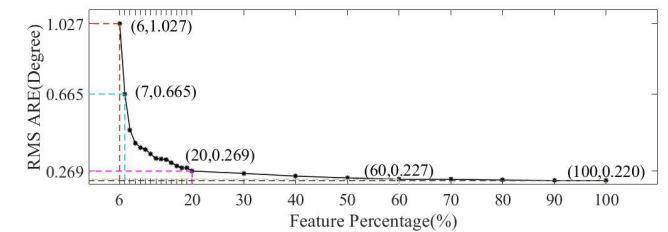


Fig. 6. RMS ARE produced by the proposed FDE-feasible LiDAR localization framework with varying feature percentages in urban canyon 1

This work will be submitted to the IEEE for possible publication. Copyright may be transferred without notice, after which this version may no longer be accessible. 9

2) Convex Property Certification for the Pose estimation model in Urban Canyon 1

This section quantifies the convexity of the planar feature-based LiDAR localization model. Its convex property is presented in the possible pose solution space from two perspectives.

(a) Convex property under different initial guesses:

For the proposed LiDAR localization pipeline, the normal initial guess of the pose at the k -th epoch is denoted as $\tilde{\mathbf{T}}_{L_k}^M$ (translation $\tilde{\mathbf{t}}_{L_k}^M$, rotation $\tilde{\mathbf{R}}_{L_k}^M$) produced by (2). The non-linear optimization of the objective function (1) is conducted based on the initial guess. Various translation initial guess $(\tilde{\mathbf{t}}_{L_k}^M)'$ with increment $\Delta \mathbf{t}$ added to $\tilde{\mathbf{t}}_{L_k}^M$ is produced as follows,

$$(\tilde{\mathbf{t}}_{L_k}^M)' = \tilde{\mathbf{t}}_{L_k}^M + \Delta \mathbf{t}. \quad (26)$$

Various rotation initial guess $(\tilde{\mathbf{R}}_{L_k}^M)'$ with increment $\Delta \mathbf{R}$ added to $\tilde{\mathbf{R}}_{L_k}^M$ is produced as follows,

$$(\tilde{\mathbf{R}}_{L_k}^M)' = \tilde{\mathbf{R}}_{L_k}^M \Delta \mathbf{R}. \quad (27)$$

The $\Delta \mathbf{R}$ is calculated from its Lie algebra $\Delta \boldsymbol{\phi}$ which could be interpreted as a rotation vector. The proposed localization pipeline with different initial guesses is elaborated in Table I.

TABLE I

NOTATIONS OF THE PROPOSED LOCALIZATION FRAMEWORK WITH DIFFERENT INITIAL GUESSES

| Name | $\Delta \mathbf{t}(\text{m})$ | $\Delta \boldsymbol{\phi}(\circ)$ | Name | $\Delta \mathbf{t}(\text{m})$ | $\Delta \boldsymbol{\phi}(\circ)$ |
|------|-------------------------------|-----------------------------------|------|-------------------------------|-----------------------------------|
| SOL0 | - | - | SOL3 | $[0 \ 0 \ 5]^T$ | - |
| SOL1 | $[5 \ 0 \ 0]^T$ | - | SOL4 | $[5 \ 5 \ 5]^T$ | - |
| SOL2 | $[0 \ 5 \ 0]^T$ | - | SOL5 | - | $[0, 0, 10]^T$ |

Note: “-” denotes no translation or rotation increment on $\tilde{\mathbf{T}}_{L_k}^M$.

For SOL0 to SOL5, the MEV of the Hessian matrix at the converged pose for each epoch is plotted in Fig. 7. Given different initial guesses, the MEV for full epochs are larger than zero with manifestation in the zoomed panel. Consequently, the strong convex property [46] of the planar feature-based localization model in the possible pose solution space is maintained.

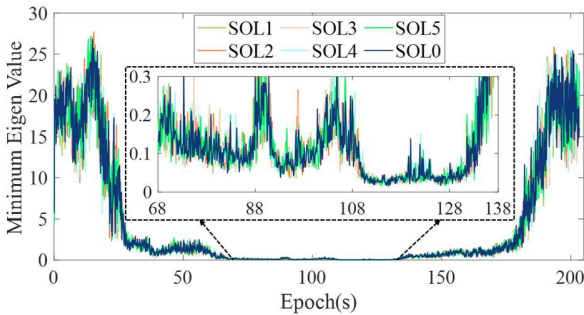


Fig. 7. The minimum eigenvalue of the Hessian matrix at the converged pose at each epoch given different initial guesses in urban canyon 1

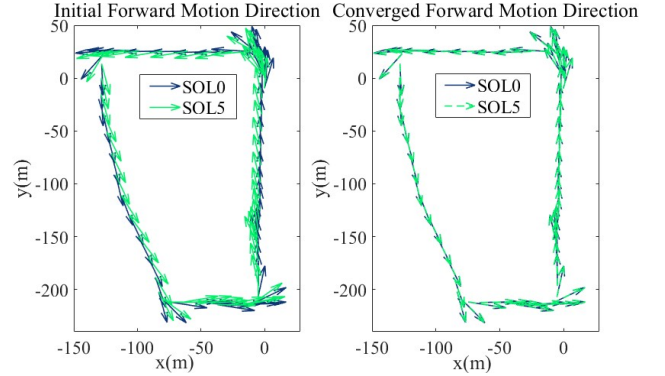


Fig. 8. The illustration of the initial forward motion direction (left) and the converged forward motion direction (right) produced by SOL0 and SOL5 in urban canyon 1

The iterative process under different rotation initial guess is displayed to further investigate the convex property of the localization model. Fig. 8 plots the initial and the converged forward motion direction of the vehicle from SOL0 and SOL5. As shown in the left panel, the initial forward motion direction of SOL0 rotates 10° counterclockwise to produce that of SOL5. As shown in the right panel, after convergence, the forward motion direction produced by SOL0 and SOL5 are almost the same.

In summary, with different initial guesses, the PD holds for the converged poses. The convex property of the adopted planar feature-based LiDAR localization model in the possible pose solution space is demonstrated in this perspective.

(b) Convex property around the converged pose solution:

The definiteness of the Hessian matrix at the pose solution $(\hat{\mathbf{T}}_{L_k}^M)'$ around the converged poses $\hat{\mathbf{T}}_{L_k}^M$ (translation $\hat{\mathbf{t}}_{L_k}^M$, rotation $\hat{\mathbf{R}}_{L_k}^M$) is investigated to analyze the convex property of the proposed localization model. Fig. 9 illustrates the MEV of the Hessian matrix in the solution space constructed by multiple $(\hat{\mathbf{T}}_{L_k}^M)'$ at the certain epoch $k = 110$ s.

For the sake of figure illustration, the 2-dimensional heatmaps are utilized. $(\hat{\mathbf{T}}_{L_k}^M)'$ is produced by adding increments on any two dimensions of translation or rotation of $\hat{\mathbf{T}}_{L_k}^M$ successively. In each subfigure, the axis label denotes the increment thus one coordinate in the map represents one $(\hat{\mathbf{T}}_{L_k}^M)'$. In detail, $\Delta \mathbf{t}_x$ and $\Delta \boldsymbol{\phi}_x$, expressed as $[\Delta t_x, 0, 0]^T$ and $[\Delta \phi_x, 0, 0]^T$, represent the translation and rotation increment on the x -axis respectively. Other labels $\Delta \mathbf{t}_y$, $\Delta \mathbf{t}_z$, $\Delta \boldsymbol{\phi}_y$ and $\Delta \boldsymbol{\phi}_z$ are defined in the same way. For example, in the top left panel of Fig. 9, $(\hat{\mathbf{T}}_{L_k}^M)'$ is derived by adding $\Delta \mathbf{t}_x$ and $\Delta \mathbf{t}_y$ to $\hat{\mathbf{t}}_{L_k}^M$ successively as (26). In the bottom left panel of Fig. 12, $(\hat{\mathbf{T}}_{L_k}^M)'$ is derived by multiplying the rotation matrix corresponding to $\Delta \boldsymbol{\phi}_x$ and $\Delta \boldsymbol{\phi}_y$ on the right of $\hat{\mathbf{R}}_{L_k}^M$ successively as (27). $\Delta \mathbf{t}_{(\cdot)}$ and $\Delta \boldsymbol{\phi}_{(\cdot)}$ range from -1m to 1m and from -10° to 10° respectively in the experiment. The $\hat{\mathbf{T}}_{L_k}^M$ is located at the center of each subfigure, where the increment is none.

This work will be submitted to the IEEE for possible publication. Copyright may be transferred without notice, after which this version may no longer be accessible. 10

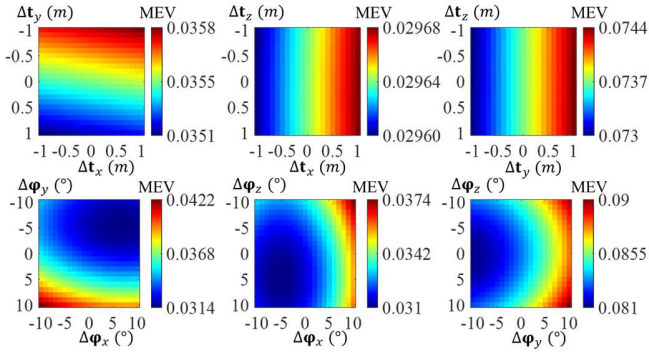


Fig. 9. The MEV of the Hessian matrix at the pose solutions around the converged one at epoch 110s in urban canyon 1. The axis label denotes the increment of the pose solution relative to the converged one. $\Delta \mathbf{t}_{(\cdot)}$ and $\Delta \boldsymbol{\phi}_{(\cdot)}$ denotes translation and rotation increment respectively on the dimension specified by the subscript (\cdot) . The MEV is mapped to color referring to the color bar.

The MEV at each $(\hat{\mathbf{T}}_{L_k}^M)'$ is mapped to color referring to the color bar. Though MEV varies with different increments, they are positive without exception. The PD of the Hessian matrix in the solution space around the converged pose is demonstrated. The same result is found for full epochs.

In summary, the objective function is in the descending direction from the neighbors of the converged pose to the converged pose itself. The cost of the objective function is proved to be minimized at the converged pose. The convex property of the adopted planar feature-based LiDAR localization model around the converged pose is demonstrated in this perspective.

3) PL Quantification in the Urban Canyon 1

For the pose estimated by the proposed LiDAR localization pipeline, the calculated PL is presented in this section. As derived in section V. B, the PL depends on the selection of the weight matrix \mathbf{W}_k . \mathbf{W}_k is the inverse of \mathbf{Q}_k which is determined by the LiDAR ranging precision. It's noted that the adopted LiDAR HDL-32E achieves measurements with centimeter-level precision. In the ideal case without dynamic objects and motion distortion, the ranging precision is declared as 2 cm [47]. On the one hand, considering the complexity of the urban scenario, the \mathbf{W}_k is first determined with the ranging precision taken as 6 cm. The PL, “3-sigma” and the APE are compared and discussed. On the other hand, the performances of PL calculated with various precision namely various weight matrices are investigated.

Fig. 10 (a) shows the PL, “3-sigma”, and APE on lateral and longitudinal translation estimates, and the orientation estimate. For the 3 components, the “3-sigma” drawn in blue is smaller than the APE drawn in green at numerous epochs. Table II further counts the percentage of epochs when “3-sigma” is larger than APE denoted by the item “3-sigma>APE (%)”. Except for the translation on the z-axis, “3-sigma>APE (%)” is lower than 35% for other pose components. It's indicated that “3-sigma” is insufficient for safety quantification. The safety hazard that APE exceeds the maximum tolerance while “3-sigma” is unaware probably occurs. The PL drawn in red is generally larger than the APE. Table II counts the percentage of

epochs when PL is larger than APE denoted by the item “PL>APE (%)”. For each of the 6d pose components, the percentage is larger than 70%, significantly higher compared with “3-sigma>APE (%)”. In other words, a large proportion of PL envelops APE. In this sense, PL is more capable of capturing the situation where APE is too large to satisfy safety requirements. In conclusion, the PL outperforms “3-sigma” for safety quantification.

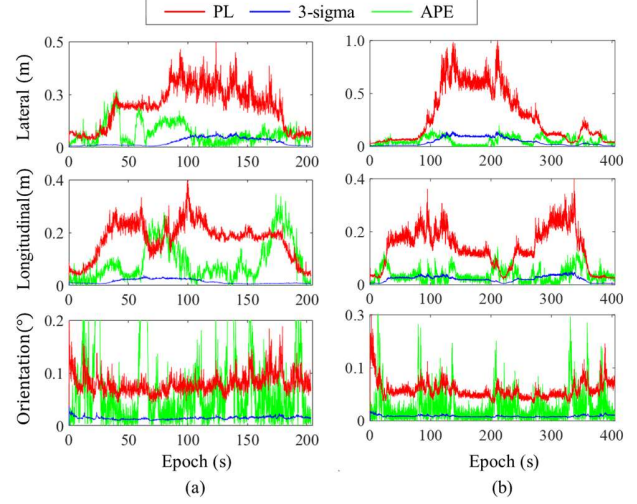


Fig. 10. The PL, “3-sigma”, and APE for lateral and longitudinal translation estimates, and the orientation estimate. (a) urban canyon 1. (b) urban canyon 2.

TABLE II
“PL>APE(%)” AND “3-SIGMA>APE(%)” FOR THE 6 POSE COMPONENTS IN URBAN CANYON 1

| Pose Component | PL>APE(%) | 3-sigma>APE(%) |
|----------------|-----------|----------------|
| Translation | x-axis | 87.95 |
| | y-axis | 78.56 |
| | z-axis | 99.71 |
| Rotation | x-axis | 87.22 |
| | y-axis | 87.32 |
| | z-axis | 70.75 |

Nevertheless, it should be noted that the PL fails to reflect the APE tightly. Taking the orientation estimate as an example, the epochs when PL is smaller than APE make up 30%. This estimation is dominated by the registration of points in the horizontal direction of the LiDAR body. The points have high resolution. Moreover, it's sensitive to orientation estimation thus providing healthy constraints. The derived PL is consequently conservative.

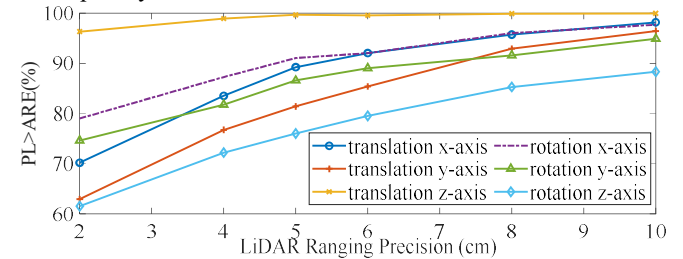


Fig. 11. The “PL>ARE(%)” for each component of the 6d pose changes concerning the LiDAR ranging precision in urban canyon 1.

This work will be submitted to the IEEE for possible publication. Copyright may be transferred without notice, after which this version may no longer be accessible. 11

Fig. 11 illustrates “PL>APE (%)” concerning the LiDAR ranging precision. Theoretically, measurements with higher precision produce pose estimations with smaller potential errors, whereas measurements with lower precision produce pose estimations with larger potential errors. The proposed PL calculation method exhibits consistency with this principle. For each component of the 6d pose, the “PL>APE (%)” gradually increased with the precision decreased from 2 cm to 10 cm. With higher precision, the derived PL is relatively small. Consequently, the epochs of “PL>APE” make up a lower percentage. With lower precision, the derived PL is relatively large. Thus, the epochs of “PL>APE” make up a higher percentage.

In conclusion, the LiDAR ranging precision is proven of noticeable importance to the performance of the PL. The weight matrix is determined by the precision in this paper. The delicate design of the weight matrix should explicitly consider measurement errors besides measurement noise. It's expected to produce the PL reflecting the APE tightly.

C. Experimental Results in Urban Canyon 2

To further verify the performance of the proposed method, another experiment was conducted in a denser urban canyon 2. The results are directly in line with the previous one.

1) Pose Estimation Accuracy in Urban Canyon 2

TABLE III
RMS APE OF THE PROPOSED LiDAR POSE ESTIMATION
METHOD IN URBAN CANYON 2

| Feature Percentage (%) | RMS ATE (m) | RMS ARE (°) |
|------------------------|-------------|-------------|
| 6 | 0.128 | 0.368 |
| 7 | 0.116 | 0.297 |
| 10 | 0.108 | 0.267 |
| 20 | 0.093 | 0.139 |
| 40 | 0.093 | 0.133 |
| 60 | 0.092 | 0.128 |
| 80 | 0.091 | 0.127 |
| 100 | 0.091 | 0.124 |

The RMS APE of the pose estimations from the proposed pipeline referring to the feature percentage is summarized in Table III. With the feature percentage increases from 6% to 20%, both RMS ATE and RMS ARE are improved significantly. While the feature percentage exceeds 20%, a slight improvement is achieved. In summary, the monotonicity and sub-modularity of the spectrum gains of the information matrix concerning the feature number during the translation and rotation estimation are demonstrated again in urban canyon 2. Moreover, the 20% cardinality restriction in Algorithm 1 is also effective for urban canyon 2. The localization method exploiting a representative subset of features rather than all the available features guarantees both accurate estimation and feasible FDE.

2) Convex Property Certification for the Pose estimation model in Urban Canyon 2

This section presents that the convex property of the planar feature-based LiDAR localization model holds in the possible

pose solution space from two perspectives in urban canyon 2.

(a) Convex property under different initial guess:

The proposed localization framework with different initial guesses is named in Table IV. Compared with the experiment on urban canyon 1, larger pose increments are exploited.

TABLE IV
SOLUTION NOTATIONS OF THE PROPOSED LOCALIZATION
FRAMEWORK WITH A DIFFERENT INITIAL GUESS FOR URBAN
CANYON 2

| Name | $\Delta t(m)$ | $\Delta \phi(^{\circ})$ | Name | $\Delta t(m)$ | $\Delta \phi(^{\circ})$ |
|------|------------------|-------------------------|------|--------------------|-------------------------|
| SOL0 | - | - | SOL3 | $[0 \ 0 \ 30]^T$ | - |
| SOL1 | $[30 \ 3 \ 0]^T$ | - | SOL4 | $[30 \ 30 \ 30]^T$ | - |
| SOL2 | $[0 \ 30 \ 0]^T$ | - | SOL5 | - | $[0, 0, 30]^T$ |

Note: “-” denotes no translation or rotation increment on $\tilde{T}_{L_k}^M$.

For SOL0 to SOL5, the MEV of the Hessian matrix at the converged pose for each epoch is plotted in Fig. 12. Given different initial guesses, the minimum eigenvalues for full epochs are positive.

The iterative process under different translation initial guesses is displayed to further investigate the convex property of the localization model. Fig. 13 plots the initial trajectory and the converged trajectory from SOL0 and SOL1 respectively. As shown in the left panel, there are 30m along the x-axis between the initial trajectories of SOL0 and SOL1. As shown in the right panel, the converged trajectories of the two solutions overlapped. The convex property of the localization model given different initial guesses is validated in urban canyon 2.

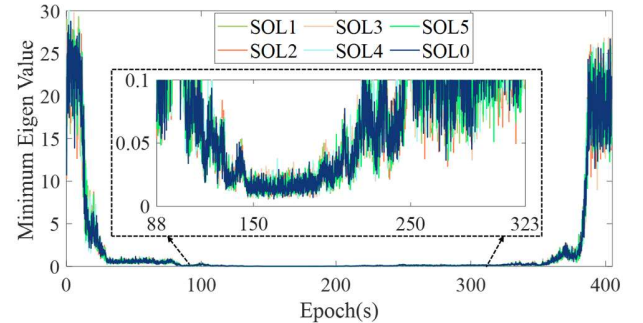


Fig. 12. The minimum eigenvalue of the Hessian matrix at the converged pose for each epoch given different initial guesses of optimization in urban canyon 2

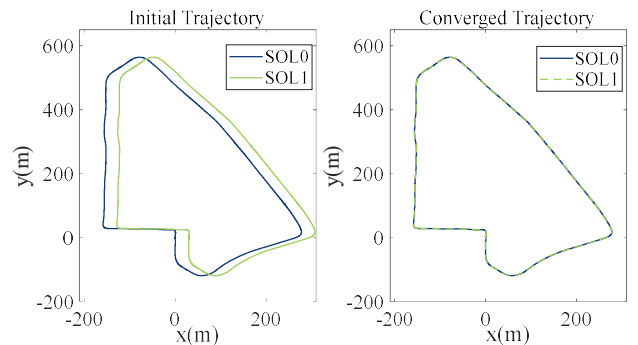


Fig. 13. The initial trajectory (left) and the converged trajectory (right) produced by SOL0 and SOL1 in urban canyon 2.

(b) Convex property around the converged pose solution:

This work will be submitted to the IEEE for possible publication. Copyright may be transferred without notice, after which this version may no longer be accessible. 12

Fig. 14 illustrates the MEV of the Hessian matrix in the pose solution space around the converged pose at the epoch 150 s. The figure labels have the same definition as that of Fig. 9.

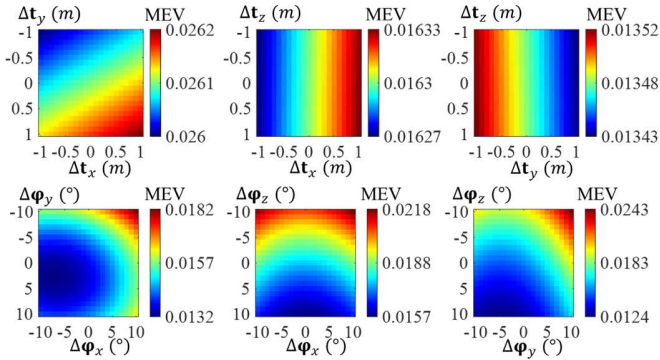


Fig. 14. The MEV of the Hessian matrix at the pose solutions around the converged one at epoch 150s in urban canyon 2. The axis label denotes the increment of the pose solutions relative to the converged one. $\Delta \mathbf{t}_{(\cdot)}$ and $\Delta \boldsymbol{\phi}_{(\cdot)}$ denotes translation and rotation increment respectively on the dimension specified by the subscript (\cdot). The MEV is mapped to color referring to the color bar.

All the MEVs are positive. The Hessian matrixes at the pose solutions around the converged pose have PD. The objective function would descend with the pose state iteratively updated from the surrounding ones to the converged one. The convex property of the localization model around the converge pose is validated in urban canyon 2.

3) PL Quantification in Urban Canyon 2

This section presents the calculated PL for the pose estimations in urban canyon 2. Fig. 10 (b) shows the PL, “3-sigma” and APE for lateral and longitudinal translation estimates and the orientation estimate. At numerous epochs, “3-sigma” is smaller than the APE while PL envelops the APE. Table V counts the percentage of “PL>APE” and “3-sigma>APE”. For all the 6 pose components, the “PL>APE (%)” is significantly larger than “3-sigma>APE (%)”. The proposed PL method outperforms “3-sigma” for safety quantification in urban canyon 2.

Yet the PL still couldn’t reflect the APE tightly. In particular, the PL is significantly larger than the APE for the translation components. The current FDE method is subject to the Gaussian assumption which is not enough practically. The remaining faults in the measurement model, which failed to be neither excluded in the FDE procedure nor considered by the single fault assumption, result in such PL.

Fig.15 illustrates “PL>APE (%)” concerning the LiDAR ranging precision in urban canyon 2. For each component of the 6d pose, the percentage increases with the decrease of the precision. The same conclusions are reached as the experiment in urban canyon 1.

TABLE V
“PL>APE(%)” AND “3-SIGMA>APE(%)” FOR THE 6 POSE COMPONENTS IN URBAN CANYON 2

| Pose Component | | PL>APE(%) | 3-sigma>APE(%) |
|----------------|--------|-----------|----------------|
| Translation | x-axis | 90.51 | 33.42 |
| | y-axis | 85.52 | 33.37 |

| | | | |
|----------|--------|-------|-------|
| Rotation | z-axis | 99.58 | 89.57 |
| | x-axis | 95.82 | 36.93 |
| | y-axis | 96.02 | 28.74 |
| | z-axis | 89.32 | 30.57 |

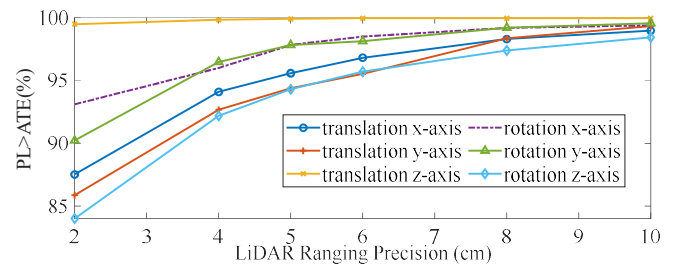


Fig. 15. The “PL>APE(%)” for each component of the 6d pose changes concerning the LiDAR ranging precision in urban canyon 2.

VII. CONCLUSION

Reliable and accurate localization is critical for the realization of intelligent vehicles. This paper aims to quantify the safety of the localization results for IV in urban canyons. Given a prior map, a safety-quantified planar feature-based LiDAR localization method is proposed.

The safety quantification method inheriting from that of satellite navigation contains two steps namely FDE and PL calculation. Representative planar features with maximum spectral attribution are selected to perform the localization. The quantity reduction of the feature enables feasible FDE. The experiments show that the localization accuracy exploiting representative features is comparable with the conventional SOTA pipeline exploiting all the available features. Hardly any accuracy compromise is caused.

Moreover, the convexity of the proposed LiDAR localization model is quantified through PD analysis of the Hessian matrix. The optimal pose estimation in the large possible pose solution space is provided given the measurements. It’s indicated that the subsequent safety quantification accounting for the noise and the undetected fault in the measurement model is credible. Based on the parity space approach, planar features with large residuals are considered as faults and iteratively excluded. The residual-based PL for each component of the 6d pose is quantified respectively. The proposed PL is demonstrated to outperform the conventional “3-sigma” for safety awareness.

Since the PL couldn’t reflect the APE tightly, the FDE combined with weight matrix estimation [48] will be proposed. The faulty measurements should be excluded via low weights and thus produce accurate pose estimation and tight PL results. Such a combination is beyond Gaussian distribution. More importantly, the localization of real-world data suffers from intractable faults. For example, the fault of the planar patch obtained from the prior map is hard to quantify. Fortunately, the source, format, and value of the faults can be customized via simulation. To formulate the PL induced by intractable faults, an investigation of the safety quantification method on the simulated real-life driving dataset [49] will be necessarily performed. Moreover, pure LiDAR localization won’t be safe under feature-insufficient scenarios and bad weather [50].

This work will be submitted to the IEEE for possible publication. Copyright may be transferred without notice, after which this version may no longer be accessible. 13

LiDAR/inertial/GNSS integrated localization leveraging the complementarity of multiple sensors is demonstrated to provide robust and accurate results in such cases [51, 52]. The safety quantification for fused localization will be explored in future work.

ACKNOWLEDGEMENT

The authors thank Mr. Xiao Xia for providing valuable theoretical instruction for preparing the manuscript.

APPENDIX

A. Derivation of the Gradient Matrix and the Hessian Matrix of $f_i(\cdot)$ Relative to \mathbf{p}_i^M

As the weighting is constant, it's omitted in the following derivation for clarity. The gradient matrix $\mathbf{G}_{\mathbf{p}^M}^f$ is derived as

$$\begin{aligned}\mathbf{G}_{\mathbf{p}^M}^f &= \frac{\partial f_i(\mathbf{p}_{k,i}^M)}{\partial \mathbf{p}_{k,i}^M} = \frac{\partial (\frac{1}{2} \mathbf{r}_{k,i}^T \mathbf{r}_{k,i})}{\partial \mathbf{p}_{k,i}^M} \\ &= \frac{\partial (\frac{1}{2} \mathbf{r}_{k,i}^T \mathbf{r}_{k,i})}{\partial \mathbf{r}_{k,i}} \frac{\partial \mathbf{r}_{k,i}}{\partial \mathbf{p}_{k,i}^M} = \mathbf{r}_{k,i} \mathbf{n}_{k,i}^T.\end{aligned}\quad (28)$$

The Hessian matrix $\mathbf{H}_{\mathbf{p}^M}^f$ is derived as

$$\mathbf{H}_{\mathbf{p}^M}^f = \frac{\partial \mathbf{G}_{\mathbf{p}^M}^f}{\partial (\mathbf{p}_{k,i}^M)^T} = \frac{\partial \mathbf{r}_{k,i} \mathbf{n}_{k,i}^T}{\partial (\mathbf{p}_{k,i}^M)^T} = \mathbf{n}_{k,i} \frac{\partial \mathbf{r}_{k,i}}{\partial (\mathbf{p}_{k,i}^M)^T} = \mathbf{n}_{k,i} \mathbf{n}_{k,i}^T. \quad (29)$$

B. Derivation of the Jacobian Matrix of $\mathbf{p}_{k,i}^M$ Relative to \mathbf{x}_k

The Jacobian matrix denoted as $\mathbf{D}_{\mathbf{x}}^{\mathbf{p}^M}$ is derived according to the left disturbance [53] manner as follows,

$$\mathbf{D}_{\mathbf{x}}^{\mathbf{p}^M} = \frac{\partial \mathbf{p}_{k,i}^M}{\partial \mathbf{x}_k^T} = \frac{\partial (\mathbf{T}_{L_k}^M \mathbf{p}_i^{L_k})}{\partial \mathbf{x}_k^T} = \lim_{\delta \mathbf{x}_k \rightarrow \mathbf{0}} \frac{\delta \mathbf{T}_{L_k}^M (\mathbf{T}_{L_k}^M \mathbf{p}_i^{L_k}) - \mathbf{T}_{L_k}^M \mathbf{p}_i^{L_k}}{\delta \mathbf{x}_k^T}, \quad (30)$$

where the minor increment of the pose is denoted as

$$\delta \mathbf{x}_k^T = \begin{bmatrix} \delta \boldsymbol{\varphi}_{L_k}^M \\ \delta \mathbf{t}_{L_k}^M \end{bmatrix}, \quad (31)$$

and equally as

$$\delta \mathbf{T}_{L_k}^M = \begin{bmatrix} \exp(\delta \boldsymbol{\varphi}_{L_k}^M) & \delta \mathbf{t}_{L_k}^M \\ \mathbf{0} & \mathbf{1} \end{bmatrix}, \quad (32)$$

where the $\delta \boldsymbol{\varphi}_{L_k}^M$ represents the skew-symmetric matrix of the $\delta \boldsymbol{\varphi}_{L_k}^M$. Substituting the increment to (29), $\mathbf{D}_{\mathbf{x}}^{\mathbf{p}^M}$ is further derived as

$$\begin{aligned}\mathbf{D}_{\mathbf{x}}^{\mathbf{p}^M} &= \lim_{\delta \mathbf{x}_k \rightarrow \mathbf{0}} \frac{(\exp(\delta \boldsymbol{\varphi}_{L_k}^M)) (\mathbf{T}_{L_k}^M \mathbf{p}_i^{L_k}) + \delta \mathbf{t}_{L_k}^M - (\mathbf{T}_{L_k}^M \mathbf{p}_i^{L_k})}{\delta \mathbf{x}_k^T} \\ &= \lim_{\delta \mathbf{x}_k \rightarrow \mathbf{0}} \frac{(\mathbf{1} + \delta \boldsymbol{\varphi}_{L_k}^M) (\mathbf{T}_{L_k}^M \mathbf{p}_i^{L_k}) + \delta \mathbf{t}_{L_k}^M - (\mathbf{T}_{L_k}^M \mathbf{p}_i^{L_k})}{\begin{bmatrix} (\delta \boldsymbol{\varphi}_{L_k}^M)^T & (\delta \mathbf{t}_{L_k}^M)^T \end{bmatrix}} \\ &= \begin{bmatrix} -(\mathbf{T}_{L_k}^M \mathbf{p}_i^{L_k})^\wedge & \mathbf{1} \end{bmatrix}.\end{aligned}\quad (33)$$

C. Derivation of the PL Induced by Gaussian Noise $\boldsymbol{\Omega}_{k,\eta}$

The LiDAR planar feature registration residual disturbed only by Gaussian noise is formulated as follows,

$$\mathbf{r}_k = \mathbf{J}_k \mathbf{x}_k + \boldsymbol{\eta}_k, \quad (34)$$

which is the same as (4) with the \mathbf{b}_k eliminated. The error in the estimated $\hat{\mathbf{x}}_k$ denoted as $\delta \hat{\mathbf{x}}_k$ is derived as

$$\delta \hat{\mathbf{x}}_k = \mathbf{J}_k^+ (\mathbf{r}_k - \mathbf{J}_k \hat{\mathbf{x}}_k - \boldsymbol{\eta}_k), \quad (35)$$

where \mathbf{J}_k^+ represents the pseudo-inverse matrix of \mathbf{J}_k . As $\boldsymbol{\eta}_k \sim \mathcal{N}(\mathbf{0}, \mathbf{Q}_k)$, $\delta \hat{\mathbf{x}}_k$ is subject to Gaussian distribution as with the mean and the covariance denoted as $\boldsymbol{\mu}_{\delta \hat{\mathbf{x}}_k}$ and $\boldsymbol{\Sigma}_{\delta \hat{\mathbf{x}}_k}$ respectively. According to the linear transformation rule of the Gaussian distribution, $\boldsymbol{\mu}_{\delta \hat{\mathbf{x}}_k}$ is derived as

$$\boldsymbol{\mu}_{\delta \hat{\mathbf{x}}_k} = \mathbf{J}_k^+ (\mathbf{r}_k - \mathbf{J}_k \hat{\mathbf{x}}_k). \quad (36)$$

The $\boldsymbol{\Sigma}_{\delta \hat{\mathbf{x}}_k}$ is derived based on the definition of covariance as follows,

$$\boldsymbol{\Sigma}_{\delta \hat{\mathbf{x}}_k} = \mathbb{E} [(\delta \hat{\mathbf{x}}_k - \boldsymbol{\mu}_{\delta \hat{\mathbf{x}}_k})(\delta \hat{\mathbf{x}}_k - \boldsymbol{\mu}_{\delta \hat{\mathbf{x}}_k})^T], \quad (37)$$

where $\mathbb{E}[\cdot]$ represents the expectation. Substituting (34) and (35) into (36), $\boldsymbol{\Sigma}_{\delta \hat{\mathbf{x}}_k}$ is further derived as

$$\boldsymbol{\Sigma}_{\delta \hat{\mathbf{x}}_k} = \mathbb{E}[(\mathbf{J}_k^+ \boldsymbol{\eta}_k)(\mathbf{J}_k^+ \boldsymbol{\eta}_k)^T] = \mathbf{J}_k^+ \mathbb{E}[\boldsymbol{\eta}_k \boldsymbol{\eta}_k^T] \mathbf{J}_k^+ = \mathbf{J}_k^+ \mathbf{Q}_k \mathbf{J}_k^+. \quad (38)$$

The inverse of $\boldsymbol{\Sigma}_{\delta \hat{\mathbf{x}}_k}$ could be expressed as

$$\boldsymbol{\Sigma}_{\delta \hat{\mathbf{x}}_k}^{-1} = (\mathbf{J}_k^+ \mathbf{Q}_k \mathbf{J}_k^+)^{-1} = \mathbf{J}_k \mathbf{W}_k \mathbf{J}_k^T. \quad (39)$$

Consequently, $\boldsymbol{\Sigma}_{\delta \hat{\mathbf{x}}_k} = (\mathbf{J}_k \mathbf{W}_k \mathbf{J}_k^T)^{-1}$ and $\boldsymbol{\Omega}_{k,\eta}$ is defined as the commonly used "3-sigma" rule that is the triple standard deviation of $\delta \hat{\mathbf{x}}_k$ thus expressed as $3\sqrt{\text{diag}((\mathbf{J}_k^T \mathbf{W}_k \mathbf{J}_k)^{-1})}$ in (17)

REFERENCES

- [1] G. Bresson, Z. Alsayed, L. Yu, and S. Glaser, "Simultaneous localization and mapping: A survey of current trends in autonomous driving," *IEEE Transactions on Intelligent Vehicles*, vol. 2, no. 3, pp. 194-220, 2017.
- [2] L. Luo, S.-Y. Cao, Z. Sheng, and H.-L. Shen, "LiDAR-based global localization using histogram of orientations of principal normals," *IEEE Transactions on Intelligent Vehicles*, vol. 7, no. 3, pp. 771-782, 2022.
- [3] Y. Zhong, F. Huang, J. Zhang, W. Wen, and L. T. Hsu, "Low - cost solid - state LiDAR/inertial - based localization with prior map for autonomous systems in urban scenarios," *IET Intelligent Transport Systems*, vol. 17, no. 3, pp. 474-486, 2023.
- [4] W. Wen, L.-T. Hsu, and G. Zhang, "Performance analysis of NDT-based graph SLAM for autonomous vehicle in diverse typical driving scenarios of Hong Kong," *Sensors-Basel*, vol. 18, no. 11, p. 3928, 2018.
- [5] T. Shan, B. Englot, C. Ratti, and D. Rus, "Lvi-sam: Tightly-coupled lidar-visual-inertial odometry via smoothing and mapping," in *2021 IEEE international conference on robotics and automation (ICRA)*, 2021: IEEE, pp. 5692-5698.
- [6] H. Yang, P. Antonante, V. Tzoumas, and L. Carlone, "Graduated non-convexity for robust spatial perception: From non-minimal solvers to global outlier rejection," *IEEE Robotics and Automation Letters*, vol. 5, no. 2, pp. 1127-1134, 2020.
- [7] T. G. Reid *et al.*, "Localization requirements for autonomous vehicles," *arXiv preprint arXiv:1906.01061*, 2019.
- [8] 'ISO 26262: Road vehicles -- Functional safety' *International Standard ISO/FDIS 26262*, ISO, 2011.
- [9] N. Joubert, T. G. Reid, and F. Noble, "Developments in modern GNSS and its impact on autonomous vehicle architectures," in *2020 IEEE Intelligent Vehicles Symposium (IV)*, 2020: IEEE, pp. 2029-2036.
- [10] R. G. Brown, "A baseline GPS RAIM scheme and a note on the equivalence of three RAIM methods," *Navigation*, vol. 39, no. 3, pp. 301-316, 1992.
- [11] M. Tossaint *et al.*, "The Stanford-ESA integrity diagram: A new tool for the user domain SBAS integrity assessment," *Navigation*, vol. 54, no. 2, pp. 153-162, 2007.
- [12] J. Blanch, T. Walter, and P. Enge, "RAIM with optimal integrity and continuity allocations under multiple failures," *IEEE Transactions on Aerospace and Electronic Systems*, vol. 46, no. 3, pp. 1235-1247, 2010.
- [13] S. Pullen and M. Joerges, "GNSS Integrity and Receiver Autonomous Integrity Monitoring (RAIM)," *Position, Navigation, and Timing*

This work will be submitted to the IEEE for possible publication. Copyright may be transferred without notice, after which this version may no longer be accessible. 14

- Technologies in the 21st Century: Integrated Satellite Navigation, Sensor Systems, and Civil Applications*, vol. 1, pp. 591-617, 2020.
- [14] M. Elhousni and X. Huang, "A survey on 3d lidar localization for autonomous vehicles," in *2020 IEEE Intelligent Vehicles Symposium (IV)*, 2020: IEEE, pp. 1879-1884.
 - [15] M. Joerger and B. Pervan, "Fault detection and exclusion using solution separation and chi-squared ARAIM," *IEEE Transactions on Aerospace and Electronic Systems*, vol. 52, no. 2, pp. 726-742, 2016.
 - [16] A. Segal, D. Hachnel, and S. Thrun, "Generalized-icp," in *Robotics: science and systems*, 2009, vol. 2, no. 4: Seattle, WA, p. 435.
 - [17] J. Zhang and S. Singh, "Low-drift and real-time lidar odometry and mapping," *Autonomous Robots*, vol. 41, no. 2, pp. 401-416, 2017.
 - [18] T. Walter and P. Enge, "Weighted RAIM for precision approach," in *PROCEEDINGS OF ION GPS*, 1995, vol. 8, no. 1: Institute of Navigation, pp. 1995-2004.
 - [19] J. Jiao *et al.*, "Greedy-based feature selection for efficient lidar slam," in *2021 IEEE International Conference on Robotics and Automation (ICRA)*, 2021: IEEE, pp. 5222-5228.
 - [20] Y. Zhao and P. A. Vela, "Good feature matching: toward accurate, robust vo/vslam with low latency," *IEEE Transactions on Robotics*, vol. 36, no. 3, pp. 657-675, 2020.
 - [21] L. Carlone and S. Karaman, "Attention and anticipation in fast visual-inertial navigation," *IEEE Transactions on Robotics*, vol. 35, no. 1, pp. 1-20, 2018.
 - [22] M. Joerger and B. Pervan, "Quantifying safety of laser-based navigation," *IEEE Transactions on aerospace and electronic systems*, vol. 55, no. 1, pp. 273-288, 2018.
 - [23] G. D. Arana, M. Joerger, and M. Spenko, "Local nearest neighbor integrity risk evaluation for robot navigation," in *2018 IEEE International Conference on Robotics and Automation (ICRA)*, 2018: IEEE, pp. 2328-2333.
 - [24] G. D. Arana, M. Joerger, and M. Spenko, "Efficient integrity monitoring for kf-based localization," in *2019 International Conference on Robotics and Automation (ICRA)*, 2019: IEEE, pp. 6374-6380.
 - [25] M. Joerger and B. Pervan, "Kalman filter-based integrity monitoring against sensor faults," *Journal of Guidance, Control, and Dynamics*, vol. 36, no. 2, pp. 349-361, 2013.
 - [26] C. Tanil, S. Khanafseh, M. Joerger, and B. Pervan, "Sequential integrity monitoring for Kalman filter innovations-based detectors," in *Proceedings of the 31st International Technical Meeting of the Satellite Division of The Institute of Navigation (ION GNSS+ 2018)*, 2018, pp. 2440-2455.
 - [27] G. D. Arana, O. A. Hafez, M. Joerger, and M. Spenko, "Recursive integrity monitoring for mobile robot localization safety," in *2019 International Conference on Robotics and Automation (ICRA)*, 2019: IEEE, pp. 305-311.
 - [28] G. Duenas Arana, O. Abdul Hafez, M. Joerger, and M. Spenko, "Integrity monitoring for Kalman filter-based localization," *The International Journal of Robotics Research*, vol. 39, no. 13, pp. 1503-1524, 2020.
 - [29] O. A. Hafez, M. Joerger, and M. Spenko, "How Safe is Particle Filtering-based Localization for Mobile Robots? An Integrity Monitoring Approach," *IEEE Transactions on Robotics*, 2024.
 - [30] H. Wang, C. Wang, C.-L. Chen, and L. Xie, "F-loam: Fast lidar odometry and mapping," in *2021 IEEE/RSJ International Conference on Intelligent Robots and Systems (IROS)*, 2021: IEEE, pp. 4390-4396.
 - [31] J. E. Angus, "RAIM with multiple faults," *Navigation*, vol. 53, no. 4, pp. 249-257, 2006.
 - [32] L.-T. Hsu *et al.*, "UrbanNav: An open-sourced multisensory dataset for benchmarking positioning algorithms designed for urban areas," in *Proceedings of the 34th International Technical Meeting of the Satellite Division of The Institute of Navigation (ION GNSS+ 2021)*, 2021, pp. 226-256.
 - [33] T. D. Barfoot, *State estimation for robotics*. Cambridge University Press, 2017, pp. 192-196.
 - [34] J. G. Belinfante, B. Kolman, and H. A. Smith, "An introduction to Lie groups and Lie algebras, with applications," *SIAM Review*, vol. 8, no. 1, pp. 11-46, 1966.
 - [35] C. Feng, Y. Taguchi, and V. R. Kamat, "Fast plane extraction in organized point clouds using agglomerative hierarchical clustering," in *2014 IEEE International Conference on Robotics and Automation (ICRA)*, 2014: IEEE, pp. 6218-6225.
 - [36] J. J. Moré, "The Levenberg-Marquardt algorithm: implementation and theory," in *Numerical analysis*: Springer, 1978, pp. 105-116.
 - [37] S. Agarwal, K. Mierle, and T. C. S. Team, "Ceres Solver," 2023. [Online]. Available: <https://github.com/ceres-solver/ceres-solver>
 - [38] T. D. Barfoot, *State estimation for robotics*. Cambridge University Press, 2017.
 - [39] J. Zhang, M. Kaess, and S. Singh, "On degeneracy of optimization-based state estimation problems," in *2016 IEEE International Conference on Robotics and Automation (ICRA)*, 2016: IEEE, pp. 809-816.
 - [40] B. Mirzasoleiman, A. Badanidiyuru, A. Karbasi, J. Vondrák, and A. Krause, "Lazier than lazy greedy," in *Proceedings of the AAAI Conference on Artificial Intelligence*, 2015, vol. 29, no. 1.
 - [41] S. Wright and J. Nocedal, "Numerical optimization," *Springer Science*, vol. 35, no. 67-68, p. 7, 1999.
 - [42] F. Gustafsson, "Statistical signal processing approaches to fault detection," *Annual Reviews in Control*, vol. 31, no. 1, pp. 41-54, 2007.
 - [43] C. Li and S. L. Waslander, "Visual measurement integrity monitoring for UAV localization," in *2019 IEEE International Symposium on Safety, Security, and Rescue Robotics (SSRR)*, 2019: IEEE, pp. 22-29.
 - [44] M. Quigley *et al.*, "ROS: an open-source Robot Operating System," in *ICRA workshop on open source software*, 2009, vol. 3, no. 3.2: Kobe, Japan, p. 5.
 - [45] M. Grupp, "evo: Python package for the evaluation of odometry and SLAM," 2017. [Online]. Available: <https://github.com/MichaelGrupp/evo>
 - [46] S. Boyd, S. P. Boyd, and L. Vandenberghe, *Convex optimization*. Cambridge university press, 2004.
 - [47] "Velodyne LiDAR HDL-32E," <https://velodynelidar.com/products/hdl-32e/> (accessed 20 December 2022).
 - [48] P. Agarwal, G. D. Tipaldi, L. Spinello, C. Stachniss, and W. Burgard, "Robust map optimization using dynamic covariance scaling," in *2013 IEEE International Conference on Robotics and Automation*, 2013: IEEE, pp. 62-69.
 - [49] A. Dosovitskiy, G. Ros, F. Codevilla, A. Lopez, and V. Koltun, "CARLA: An open urban driving simulator," in *Conference on robot learning*, 2017: PMLR, pp. 1-16.
 - [50] L. Huang, "Review on LiDAR-based SLAM Techniques," in *2021 International Conference on Signal Processing and Machine Learning (CONF-SPML)*, 2021: IEEE, pp. 163-168.
 - [51] H. Ye, Y. Chen, and M. Liu, "Tightly coupled 3d lidar inertial odometry and mapping," in *2019 International Conference on Robotics and Automation (ICRA)*, 2019: IEEE, pp. 3144-3150.
 - [52] T. Shan, B. Englot, D. Meyers, W. Wang, C. Ratti, and D. Rus, "Lio-sam: Tightly-coupled lidar inertial odometry via smoothing and mapping," in *2020 IEEE/RSJ international conference on intelligent robots and systems (IROS)*, 2020: IEEE, pp. 5135-5142.
 - [53] J. M. Selig, "Lie groups and lie algebras in robotics," in *Computational Noncommutative Algebra and Applications*, 2004: Springer, pp. 101-125.



Jiachen Zhang was born in Cangzhou, Hebei, China. She received her B.S. and Ph.D. degrees in optoelectronic information science and engineering from School of Precision Instrument and Opto-Electronics Engineering, Tianjin University, Tianjin, China, in 2016 and 2022, respectively. She is currently a post-doctoral researcher in the Department of Aeronautical and Aviation Engineering, The Hong Kong Polytechnic University. Her research interests include LiDAR-based localization for autonomous vehicles, safety-certifiable localization, and SLAM.



Xikun Liu received his bachelor's degree in Mechanical Design, Manufacturing, and Automation from Huazhong University of Science and Technology, China in 2017, and master's degree in Mechatronics and Information Technology from Karlsruhe Institute of

This work will be submitted to the IEEE for possible publication. Copyright may be transferred without notice, after which this version may no longer be accessible. 15

Technology, Germany in 2021. He is currently pursuing a Ph.D. in the Department of Aeronautical and Aviation Engineering, the Hong Kong Polytechnic University. His research interests include GNSS and sensor-aided GNSS positioning, SLAM, and multiple sensor fusion in autonomous driving.



Weisong Wen (Member, IEEE) received a BEng degree in Mechanical Engineering from Beijing Information Science and Technology University (BISTU), Beijing, China, in 2015, and an MEng degree in Mechanical Engineering from the China Agricultural University,

in 2017. After that, he received a PhD degree in Mechanical Engineering from The Hong Kong Polytechnic University (PolyU), in 2020. He was also a visiting PhD student with the Faculty of Engineering, University of California, Berkeley (UC Berkeley) in 2018. Before joining PolyU as an Assistant Professor in 2023, he was a Research Assistant Professor at AAE of PolyU since 2021. He has published 30 SCI papers and 40 conference papers in the field of GNSS (ION GNSS+) and navigation for Robotic systems (IEEE ICRA, IEEE ITSC), such as autonomous driving vehicles. He won the innovation award from TechConnect 2021, the Best Presentation Award from the Institute of Navigation (ION) in 2020, and the First Prize in Hong Kong Section in Qianhai-Guangdong-Macao Youth Innovation and Entrepreneurship Competition in 2019 based on his research achievements in 3D LiDAR aided GNSS positioning for robotics navigation in urban canyons. The developed 3D LiDAR-aided GNSS positioning method has been reported by top magazines such as Inside GNSS and has attracted industry recognition with remarkable knowledge transfer.



Li-Ta Hsu received B.S. and Ph.D. degrees in aeronautics and astronautics from National Cheng Kung University, Taiwan, in 2007 and 2013, respectively. He is currently an associate professor with the Department of Aeronautical and Aviation Engineering, The Hong Kong Polytechnic University before he served as a post-doctoral researcher at the

Institute of Industrial Science at the University of Tokyo, Japan. In 2012, he was a visiting scholar at University College London, the U.K. His research interests include GNSS positioning in challenging environments and localization for pedestrian, autonomous driving vehicle, and unmanned aerial vehicle.